REPORT DOCUMENTATION PAGE

Form Approved OMB NO. 0704-0188

1. AGENCY USE ONLY (Leave Blank)	2. REPORT DATE:	3. REPORT TYPE AND DATES COVERED
		Final Report 18-Jul-2005 - 17-Feb-2006

4. TITLE AND SUBTITLE	5. FUNDING NUMBERS
On-Line Path Generation and Tracking for High-Speed Wheeled Autonomous Vehicles	W911NF0510331

6. AUTHORS	8. PERFORMING ORGANIZATION REPORT NUMBER
Panagiotis Tsiotras	

7. PERFORMING ORGANIZATION NAMES AND ADDRESSES

Georgia Institute of Technology
Office Of Contract Administration
Program Initiation Division
Atlanta, GA   30332 -0420

9. SPONSORING/MONITORING AGENCY NAME(S) AND ADDRESS(ES)	10. SPONSORING / MONITORING AGENCY REPORT NUMBER
U.S. Army Research Office P.O. Box 12211 Research Triangle Park, NC 27709-2211	47338-CI.1

11. SUPPLEMENTARY NOTES

The views, opinions and/or findings contained in this report are those of the author(s) and should not contrued as an official Department of the Army position, policy or decision, unless so designated by other documentation.

12. DISTRIBUTION AVAILIBILITY STATEMENT	12b. DISTRIBUTION CODE
Approved for Public Release; Distribution Unlimited	

13. ABSTRACT (Maximum 200 words)

The abstract is below since many authors do not follow the 200 word limit

14. SUBJECT TERMS	15. NUMBER OF PAGES
high speed vehicles, yaw control, optimal trajectory generation, friction circle	Unknown due to possible attachments
	16. PRICE CODE

17. SECURITY CLASSIFICATION OF REPORT	18. SECURITY CLASSIFICATION ON THIS PAGE	19. SECURITY CLASSIFICATION OF ABSTRACT	20. LIMITATION OF ABSTRACT
UNCLASSIFIED	UNCLASSIFIED	UNCLASSIFIED	UL

Report Title

On-Line Path Generation and Tracking for High-Speed Wheeled Autonomous Vehicles

ABSTRACT

In this work we proposed two semi-analytic methods to generate minimum and near-minimum time velocity profiles for a vehicle along a specified path. Initially we adopt a point mass parametrization of the vehicle with specified acceleration limits. In generating the optimal velocity profile, several undesirable cases, where loss of controllability occurs, and which have been neglected in the literature, are dealt with in this work. A receding horizon implementation is also proposed for the on-line implementation of the velocity optimizer. Robustness of the receding horizon algorithm is guaranteed by the use of an adaptive scheme that determines the planning and execution horizons. Application to a Formula 1 (F1) circuit with a comparison between the infinite and finite receding horizon schemes provides a validation of the proposed methodology. We also provide extensions from the point mass to a half-car model to recover the missing attitude (yaw) information. The acceleration limits (GG-diagram) of the half-car model is determined by the available tire friction forces in the front and rear axles. We present three extensions of the point mass methodology to the half-car model. In the first extension we directly implement the optimal control strategy of the point mass case to the half-car model. In the second extension the optimal control strategy of the point mass case is interrupted by a stabilizing control logic when the vehicle slip angle increases beyond a certain value and the yaw dynamics tend to instability. Finally, in the third approach we enforce the additional constraint that the vehicle tracks the path with zero slip angle and determine the acceptable acceleration limits subject to the new constraint.

List of papers submitted or published that acknowledge ARO support during this reporting period. List the papers, including journal references, in the following categories:

(a) Papers published in peer-reviewed journals (N/A for none)

Velenis, E., and Tsiotras P., "Minimum-Time Travel for a Vehicle with Acceleration Limits: Theoretical Analysis and Receding Horizon Implementation," Journal of Optimization Theory and Applications, (submitted January 2006).

Number of Papers published in peer-reviewed journals: 1.00

(b) Papers published in non-peer-reviewed journals or in conference proceedings (N/A for none)

Velenis, E. and Tsiotras, P., "Optimal Velocity Profile Generation for Given Acceleration Limits: Theoretical Analysis," American Control Conference, Portland, OR, June 8--10, 2005, pp. 1478--1483.

Velenis, E. and Tsiotras, P., "Optimal Velocity Profile Generation for Given Acceleration Limits: Receding Horizon Implementation," American Control Conference , Portland, OR, June 8--10, 2005, pp. 2147--2152.

Velenis, E., and Tsiotras, P., "Optimal Velocity Profile Generation for Given Acceleration Limits: The Half-Car Model Case," IEEE International Symposium on Industrial Electronics (ISIE05), Dubrovnik, Croatia, June 20-23, 2005 (invited).

Velenis, E., and Tsiotras, P., "Minimum Time vs. Maximum Exit Velocity Path Optimization During Cornering," IEEE International Symposium on Industrial Electronics (ISIE05), Dubrovnik, Croatia, June 20-23, 2005 (invited).

Number of Papers published in non peer-reviewed journals: 4.00

(c) Papers presented at meetings, but not published in conference proceedings (N/A for none)

Number of Papers not Published: 0.00

(d) Manuscripts

Number of Manuscripts: 0.00

Number of Inventions:

Graduate Students

NAME	PERCENT_SUPPORTED	
Efstathios Velenis	1.00	No
Efstathios Bakolas	1.00	No
FTE Equivalent:	**2.00**	
Total Number:	**2**	

Names of Post Doctorates

NAME	PERCENT_SUPPORTED
FTE Equivalent:	
Total Number:	

Names of Faculty Supported

NAME	PERCENT_SUPPORTED	National Academy Member
Panagiotis Tsiotras	0.10	No
FTE Equivalent:	**0.10**	
Total Number:	**1**	

Names of Under Graduate students supported

NAME	PERCENT_SUPPORTED
FTE Equivalent:	
Total Number:	

Names of Personnel receiving masters degrees

NAME
Total Number:

Names of personnel receiving PHDs

NAME	
Efstathios Velenis	No
Total Number:	**1**

Names of other research staff

FTE Equivalent:
Total Number:

Sub Contractors (DD882)

Inventions (DD882)

REPORT DOCUMENTATION PAGE

Form Approved
OMB NO. 0704-0188

1. AGENCY USE ONLY (Leave Blank)	2. REPORT DATE	3. REPORT TYPE AND DATES COVERED

4. TITLE AND SUBTITLE	5. FUNDING NUMBERS

6. AUTHOR(S)

7. PERFORMING ORGANIZATION NAME(S) AND ADDRESS(ES)	8. PERFORMING ORGANIZATION REPORT NUMBER

9. SPONSORING / MONITORING AGENCY NAME(S) AND ADDRESS(ES)	10. SPONSORING / MONITORING AGENCY REPORT NUMBER
U. S. Army Research Office P.O. Box 12211 Research Triangle Park, NC 27709-2211	

11. SUPPLEMENTARY NOTES

The views, opinions and/or findings contained in this report are those of the author(s) and should not be construed as an official Department of the Army position, policy or decision, unless so designated by other documentation.

12 a. DISTRIBUTION / AVAILABILITY STATEMENT	12 b. DISTRIBUTION CODE
Approved for public release; distribution unlimited.	

13. ABSTRACT (Maximum 200 words)

14. SUBJECT TERMS

15. NUMBER OF PAGES

16. PRICE CODE

17. SECURITY CLASSIFICATION OR REPORT **UNCLASSIFIED**	18. SECURITY CLASSIFICATION ON THIS PAGE **UNCLASSIFIED**	19. SECURITY CLASSIFICATION OF ABSTRACT **UNCLASSIFIED**	20. LIMITATION OF ABSTRACT **UL**

Standard Form 298 (Rev.2-89)
Prescribed by ANSI Std. 239-18
298-102

Enclosure 1

On-Line Path Generation and Tracking for High-Speed Wheeled Autonomous Vehicles

by

Panagiotis Tsiotras

Principal Investigator
School of Aerospace Engineering
Georgia Institute of Technology
Atlanta, GA 30332-0150

Interim Report
Period: 7/17/05 – 3/17/06

submitted to:

U.S. Army Research Office
Systems and Control
P.O. Box 12211
4300 South Miami Blvd.
Research Triangle Park, NC 27709-2211

Attention
Dr. Randy Zachery
Tel: (919) 549-4368, Fax: (919) 549-4354
Email: randy.zachery@us.army.mil

March 2006

GeorgiaInstitute
of Technology
School of Aerospace Engineering

School of Aerospace Engineering
Atlanta, Georgia 30332-0150 U.S.A.
PHONE 404-894-9526
FAX 404-894-2760

1 Abstract

Semi-analytic methods to generate minimum and near-minimum time velocity profiles for a vehicle along a specified path are presented in this report.

Initially we adopt a point mass parametrization of the vehicle with specified acceleration limits. In generating the optimal velocity profile, several undesirable cases, where loss of controllability occurs, and which have been neglected in the literature, are dealt with in this work. A receding horizon implementation is also proposed for the on-line implementation of the velocity optimizer. Robustness of the receding horizon algorithm is guaranteed by the use of an adaptive scheme that determines the planning and execution horizons. Application to a Formula 1 (F1) circuit with a comparison between the infinite and finite receding horizon schemes provides a validation of the proposed methodology.

Extensions of the point mass methodology to a half-car model are presented next in order to recover the missing attitude (yaw) information. The acceleration limits (GG-diagram) of the half-car model is determined by the available tire friction forces in the front and rear axles. We present three extensions of the point mass methodology to the half-car model. In the first extension we directly implement the optimal control strategy of the point mass case to the half-car model. In the second extension the optimal control strategy of the point mass case is interrupted by a stabilizing control logic when the vehicle slip angle increases beyond a certain value and the yaw dynamics tend to instability. Finally, in the third approach we enforce the additional constraint that the vehicle tracks the path with zero slip angle and determine the acceptable acceleration limits subject to the new constraint.

Contents

List of Figures

3

2 Statement of the Problem

Achieving autonomous operation in open terrain remains a challenging problem in the development of land vehicles. This is due to the uncertainty of the environment the vehicle operates in, as well as due to the poor characterization of the complex vehicle dynamics and their integration with sensors and actuators. A solution to this problem requires not only sophisticated hardware components (for actuation, sensing, and communication), but also advanced software algorithms and supervisory control strategies that can make use of the full capability of these components.

A class of vehicles we envision to be completely automated in the future are ground wheeled vehicles (Fig. 1(a)) that operate in hostile off-road environments (e.g., battlefields). A typical mission would be to drive the vehicle from point A to point B, avoid any obstacles, while minimizing the exposure to danger; see Fig. 1(b). In general, minimization of the exposure to danger involves driving through a trajectory in minimum time or maximum average velocity.

(a)	(b)

Figure 1: (a) autonomous military off-road vehicles will exhibit a high degree of tactical mobility, while eliminating the risk of loss of human lives; (b) a typical mission scenario will involve an autonomous vehicle entering a hazardous area to perform its mission objective, while avoiding obstacles and/or minimizing its exposure to enemy threats and countermeasures.

The objective of this research project is to built on our previous experience on the analysis of the dynamics and the optimal control of high-speed wheeled vehicles in order to develop new, advanced control methodologies for the on-line control of autonomous land vehicles that mimic the way expert humans drive. The focus of this work will be in autonomous path generation, navigation and tracking for unmanned wheeled terrestrial vehicles operating in high-speed. The emphasis on high-speed operation stems from the need to minimize reaction time and exposure to external threats. Specifically, the following problems will be addressed during this project:

2.1 Challenges

The problem of trajectory planning for high-speed autonomous vehicles is typically dealt with in the literature by means of numerical optimization. Several published results have addressed path

planning of high-speed ground vehicles [1, 2, 3, 4]. These results demonstrate that numerical techniques allow one to incorporate accurate, high order dynamical models in the optimization process, thus producing realistic results. In fact, the optimal solutions generated using these optimizers are comparable to experimental results obtained from expert race drivers [2, 3, 4]. On the other hand, these numerical optimization approaches are computationally intensive, and they cannot be readily applied in cases where the environment changes unpredictably. As a result, they are not suitable for real-time path-planning optimization.

In the work of Spenko [5] real-time trajectory planning for hazard avoidance of high-speed Unmanned Ground Vehicles (UGV's) in rough terrain has been addressed. A fairly rich vehicle model has been used to predict and avoid roll-over and excessive side-slip. The computational cost is mitigated somewhat by choosing the hazard avoidance maneuver from a library of off-line pre-computed candidates.

2.2 Approach

An alternative approach for on-line trajectory optimization of ground vehicles is proposed in this work. Having in mind the requirement for reduction of the computational cost, we are motivated to explore the possibility of solving the trajectory planning problem (or at least part of this problem) analytically or semi-analytically. We separate the geometric problem of designing the optimal path from the dynamic problem of optimally following this path given the vehicle dynamic characteristics. Specifically, we assume that the geometric characteristics of the reference trajectory are provided a priori. This means that the path to be followed will be the result of another optimization step, which will typically incorporate additional constraints, such as minimum distance traveled, minimum average curvature, or a combination of the two. Since the dynamics of the vehicle are not directly included in this optimization step, we expect a reduced computational cost. This separation of the geometric from the dynamic problem has also been proposed in [6, 7] and [8]. The path in these references is designed using geometric principles and an "intuitively optimal" velocity profile is generated using a semi-analytical approach, by taking into consideration the maximum acceleration available to the vehicle at each point on the path. Notice that in [6, 7, 8] the yaw dynamics of the vehicle are neglected. A similar problem to the one investigated in this paper has been addressed in [9], [10] and [11]. Therein the authors investigated the minimum time solution for a robotic manipulator moving its tip along a prescribed path, while taking into consideration the actuator limits. In order for all actuators to maintain enough control authority for the tip to track the desired path *exactly*, a state constraint is introduced which defines a set of admissible velocities. The proposed solution consists only of bang-bang control intervals, and the velocity profile may coincide with the allowable limit only instantaneously. Proof of optimality is provided by point-wise maximization of the velocity. The extension from point-mass to a half-car model (that includes rotation of the vehicle about its vertical axis) creates new problems. Specifically, direct implementation of the optimal strategy from the point-mass model may lead to unstable oversteer in tight corners. We propose a stabilizing strategy to remedy the instability without sacrificing performance, in terms of speed.

6

3 Summary of Results

3.1 Introduction

In this work we first concentrate on providing a rigorous proof of optimality of the approach in [6, 7, 8] for a point mass consideration of the vehicle (neglecting the yaw dynamics) using optimal control theory. We also account for the loss of controllability due to limited accelerating/braking and cornering forces. The set of admissible velocities is explicitly expressed in terms of the acceleration capacity of the vehicle and the curvature of the path to be followed. We present a solution that allows the velocity to stay within the allowable limit using alternative control strategies, in conjunction to bang-bang intervals, as necessary. In addition, a constructive proof of optimality for several special cases of paths to be followed is provided. The necessary optimality conditions are explicitly derived, which allow us to draw conclusions on the number and type of control switchings. In particular, the switching points are found semi-analytically instead of numerically (as it was done in [9], [10], [11]). Application to an F1 circuit provides a validation of the proposed methodology.

In order for a trajectory optimization scheme to be suitable for on-line implementation, it must be able to adapt to changing environments, in addition to having a reduced computational cost. In [12, 13, 14] real-time trajectory planning for autonomous (aerial) vehicles using a receding horizon scheme was proposed. In a receding horizon scheme the optimization is not performed throughout the whole trajectory, but it is rather computed from the current position up to a pre-specified horizon. The vehicle executes part of the computed optimal trajectory, while simultaneously optimizing the path up to a new horizon. The search space at each optimization step is considerably reduced, which results in reduced computational cost. In addition, the receding horizon implementation accounts for changes in the environment outside the optimization horizon for each step.

We propose a receding horizon implementation of the previous semi-analytical optimal velocity profile algorithm. The algorithm ensures that at the end of each executed subarc the vehicle can reach a "safe state" (for example, complete stop) regardless of the (a priori unknown) changes in the environment outside the planning horizon. This is achieved by designing a dynamic scheme that determines appropriate planning and execution horizons. Finally, we apply the receding horizon optimization scheme to an F1 circuit to validate our approach.

Afterwards the point mass methodology for minimum time velocity profiles is extended to a vehicle model including the yaw dynamics. A half-car model with nonlinear tire friction characteristics is introduced and the acceleration envelope (GG-diagram) of the vehicle is calculated for any operating condition. The maximum available acceleration and maximum available deceleration is determined within the GG-diagram and a direct extension of the optimal control strategy of the point mass case is proposed using the dynamics of the half-car model. Numerical simulations reveal that the stability of the yaw dynamics needs to be taken into consideration.

Stability of the yaw dynamics of passenger vehicles has been a subject of intense research in the automotive community and has led to the development of commercial active safety systems such as the Electronic Stability Program (ESP). The ESP uses individual wheel braking to generate stabilizing yaw moments in critical cases where the vehicle operates close to an estimated stability margin. In [15] this stability margin is characterized by the vehicle slip angle β. In [16] the stability margin is determined empirically in the β–$\dot{\beta}$ plane and its dependence on the velocity of the vehicle is demonstrated.

We present two approaches for a stable implementation of the control strategy for the point mass case to a half-car model. In the first approach we design stabilizing control schemes that intervene during execution of the optimal maximum acceleration/maximum deceleration action when the vehicle slip angle increases and the yaw dynamics tend to instability. In the second approach we

7

redefine the maximum acceleration limits of the vehicle subject to the additional constraint of zero vehicle slip angle throughout the path.

3.2 The Point Mass Vehicle Case

3.2.1 Problem Formulation

Consider a vehicle of mass m travelling along a prescribed path, with given acceleration limits and fixed initial and final position and velocity. We seek the velocity profile along the path for minimum travel time. The path is described by its radius $r(s)$ at each point, which is given as a function of the path length coordinate s, or equivalently by the curvature $k(s)$ along the path (Fig. 2). The cartesian coordinates at any point on the path can be calculated using the following standard transformation
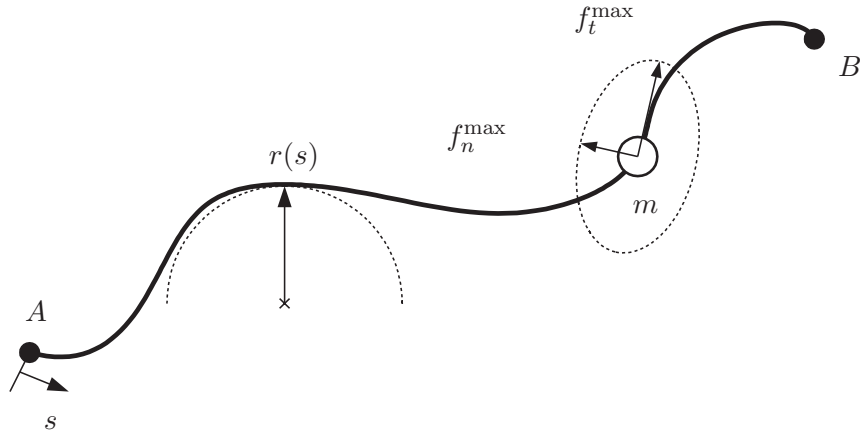
Figure 2: A vehicle of mass m travels along the prescribed path $r(s)$ with given maximum acceleration limits in minimum time.

$$k(s) \triangleq \frac{1}{r(s)}, \qquad \phi(s) \triangleq \int_{s_0}^{s} k(\sigma)\mathrm{d}\sigma,$$

$$x(s) = \int_{s_0}^{s} \cos\phi(\sigma)\mathrm{d}\sigma, \qquad y(s) = \int_{s_0}^{s} \sin\phi(\sigma)\mathrm{d}\sigma. \tag{1}$$

The equations of motion are given by

$$m\frac{\mathrm{d}^2 s}{\mathrm{d}t^2} = f_t, \qquad m\left(\frac{\mathrm{d}s}{\mathrm{d}t}\right)^2 = f_n r(s), \tag{2}$$

where, f_t is the tangential component of the force along the path, and f_n is the normal (centripetal) force such that the vehicle tracks the prescribed path. The force acting on the vehicle is limited within the ellipse

$$\left(\frac{f_t}{f_t^{\max}}\right)^2 + \left(\frac{f_n}{f_n^{\max}}\right)^2 - 1 \leq 0. \tag{3}$$

This is shown in Fig. 2, where $f_t^{\max}$ is the maximum longitudinal force and $f_n^{\max}$ is the maximum lateral force. We assume that the initial and final vehicle velocities are given, and satisfy

$$\left.\frac{\mathrm{d}s}{\mathrm{d}t}\right|_{t=t_0} < \frac{f_n^{\max} r(s_0)}{m}, \qquad \left.\frac{\mathrm{d}s}{\mathrm{d}t}\right|_{t=t_f} \leq \frac{f_n^{\max} r(s_f)}{m}, \tag{4}$$

8

in order for the initial and final cornering forces to be less than the allowable limit $f_n^{\max}$ and also in order for some accelerating/braking force f_t to be available at t_0. Moreover, it will be assumed that the velocity of the vehicle is always greater than or equal to zero, that is, $ds/dt \geq 0$ for all $t \in [t_0, t_f]$. Specifically, the vehicle is not allowed to reverse direction, a natural assumption for a minimum-time problem.

From now on, and unless stated otherwise, we assume uniform acceleration limits $f_t^{\max} = f_n^{\max} = F_{\max}$, i.e., the total force lies within a circle of radius $F_{\max}$.

Consider the following state assignment and change of time scale:

$$\tau \triangleq \beta t, \quad z_1 \triangleq \alpha\beta s, \quad z_2 \triangleq \alpha\frac{ds}{dt}, \tag{5}$$

with $\alpha \triangleq \sqrt{m/F_{\max}}$ and $\beta \triangleq \alpha F_{\max}/m$. The state-space representation of the system may then be written as

$$\dot{z}_1 = z_2, \tag{6}$$

$$\dot{z}_2 = \frac{f_t}{F_{\max}}, \tag{7}$$

where $(\dot{})$ denotes derivative with respect to τ. The control input in this formulation is f_t, and the maximum overall acceleration limit $F_{\max}/m$ translates to a state-dependent control constraint as follows

$$\left(\frac{f_t}{F_{\max}}\right)^2 + \left(\frac{z_2^2}{R(z_1)}\right)^2 - 1 \leq 0, \tag{8}$$

where $R(z_1) \triangleq r(z_1/(\alpha\beta))$.

The control constraint (8) can be written as

$$\frac{f_t}{F_{\max}} = u\sqrt{1 - \frac{z_2^4}{R^2(z_1)}}, \quad u \in [-1, +1]. \tag{9}$$

In terms of the new control variable u the dynamics of the system is written as

$$\dot{z}_1 = z_2, \quad \dot{z}_2 = u\sqrt{1 - \frac{z_2^4}{R^2(z_1)}}, \quad u \in [-1, +1]. \tag{10}$$

In terms of the original variables, the equation of motion, using the elliptic force envelope constraint (3) can be written as

$$m\frac{d^2s}{dt^2} = u\sqrt{(f_t^{\max})^2 - \frac{m}{r(s)}\left(\frac{f_t^{\max}}{f_n^{\max}}\right)^2\left(\frac{ds}{dt}\right)^2}, \tag{11}$$

where $u \in [-1, +1]$.

Note that the dynamics (10) are well defined only for trajectories inside the region $\mathcal{S} \subset \mathbb{R}^2$ of the state space defined by

$$\mathcal{S} \triangleq \{(z_1, z_2) : C_0(z_1, z_2) \triangleq z_2^2 - |R(z_1)| \leq 0\}. \tag{12}$$

In addition, controllability is maintained only at the interior of the set $\mathcal{S}$. At the boundary of the set $\mathcal{S}$ controllability is lost. The following lemma states that unless we have a path of constant curvature, the state constraint $C_0(z_1, z_2) \leq 0$ is always inactive for any finite interval of time, hence controllability is maintained for any path of nonzero curvature. In the following, $R'(z_1) = \partial R(z_1)/\partial z_1$.

9

Lemma 1 *Assume $R'(z_1) \neq 0$ for any $z_1 \in (z_\alpha, z_\beta) \subset [z_{10}, z_{1f}]$, where $z_{10} = z_1(\tau_0)$ and $z_{1f} = z_1(\tau_f)$. Then the manifold $\partial \mathcal{S} = \{(z_1, z_2) : C_0(z_1, z_2) = 0\}$ is not invariant for the system (10) for any control u.*

Proof: Invariance of $\partial \mathcal{S}$ with respect to (10) implies that

$$-\dot{z}_1 R'(z_1) \operatorname{sgn} R(z_1) + 2z_2 \dot{z}_2 = 0, \tag{13}$$

equivalently,

$$-z_2 R'(z_1) \operatorname{sgn} R(z_1) = 0, \tag{14}$$

since $\dot{z}_2 = 0$ on $\partial \mathcal{S}$ for any $u \in [-1, +1]$. Since $z_2 > 0$ for all $z_1 \in (z_{10}, z_{1f})$, the last equation is satisfied if and only if $R'(z_1) = 0$. $\blacksquare$

An immediate consequence of Lemma 1 is the fact that $\partial \mathcal{S}$ is invariant under (10) only for paths of constant curvature.

Note that the flow of the trajectories of (10) in the vicinity of the constraint $C_0(z_1, z_2) = 0$ are given by

$$\begin{aligned}
\frac{dC_0(z_1, z_2)}{dt} &= \frac{\partial C_0}{\partial z_1} \dot{z}_1 + \frac{\partial C_0}{\partial z_2} \dot{z}_2 \\
&= -\dot{z}_1 R'(z_1) \operatorname{sgn} R(z_1) + 2z_2 \dot{z}_2 \\
&= -z_2 R'(z_1) \operatorname{sgn} R(z_1).
\end{aligned}$$

It follows that

$$\frac{dC_0(z_1, z_2)}{dt} < 0, \quad \text{if} \quad R'(z_1) \operatorname{sgn} R(z_1) > 0 \tag{15}$$

and

$$\frac{dC_0(z_1, z_2)}{dt} > 0, \quad \text{if} \quad R'(z_1) \operatorname{sgn} R(z_1) < 0. \tag{16}$$

The following corollary is therefore immediate.

Corollary 1 *The set $\mathcal{S}$ is invariant for the system (10) only for paths of monotonically decreasing curvature (increasing radius). Such paths are characterized by the inequality $R'(z_1) \operatorname{sgn} R(z_1) > 0$.*

Given a certain path, characterized by its radius $R(z_1)$, the velocity z_2 for which the constraint $C_0(z_1, z_2) = 0$ is satisfied is thus of extreme importance for our problem. We will denote this velocity by $z_{2\text{crit}}(z_1)$. It is given by

$$z_{2\text{crit}}(z_1) \triangleq \sqrt{|R(z_1)|}. \tag{17}$$

When $z_2(z_1) = z_{2\text{crit}}(z_1)$ for some $z_1 \in [z_{10}, z_{1f}]$ loss of controllability ensures. Corollary 1 essentially states that for paths of monotonically decreasing curvature loss of controllability can occur only instantaneously. This can also be seen from the following simple argument. Assume, for instance, that at some point $\tau_c \in (\tau_0, \tau_f)$, $z_2(\tau_c) = z_{2\text{crit}}(z_1(\tau_c))$. The tangential component of the acceleration becomes zero and $\dot{z}_2(\tau_c) = 0$. Since the vehicle travels on a path of monotonically decreasing curvature (increasing radius), $|R(z_1(\tau_c^+))| > |R(z_1(\tau_c))|$, while $z_2(\tau_c^+) = z_2(\tau_c)$. It follows that the square root in the rhs of equation (10) will take a positive, non-zero value at $\tau = \tau_c^+$ and the system will regain controllability. For a path of monotonically increasing curvature (decreasing radius) on the other hand, the condition $z_2(\tau_c) = z_{2\text{crit}}(z_1(\tau_c))$ at some point

10

$\tau_c \in (\tau_0, \tau_f)$ leads to $\dot{z}_2(\tau_c) = 0$ and $z_2(\tau_c^+) = z_2(\tau_c)$, and since $|R(z_1(\tau_c^+))| < |R(z_1(\tau_c))|$, it follows that $z_2^2(\tau_c^+) \geq |R(z_1(\tau_c^+))|$. The quantity inside the square root at the right-hand-side of (10) becomes negative at τ_c^+. The equations are infeasible and a larger centripetal force than the available one $F_{\max}$ is needed for the vehicle to negotiate the path. It follows that for a path of monotonically increasing curvature (characterized by the inequality $R'(z_1) \operatorname{sgn} R(z_1) < 0$) we cannot allow the vehicle to reach $z_{2\mathrm{crit}}(z_1)$. In Section 3.2.5 we discuss this case in great detail and we show that optimal paths necessarily remain in $\mathcal{S}$.

We know turn to the solution of the minimum time problem for system (10).

3.2.2 Optimal Control Formulation

In reference to the system (10), and given fixed initial conditions $z_{10} = z_1$, $z_{20} = z_2$ at $\tau = \tau_0$ and final condition $z_{1f} = z_1$, $z_{2f} = z_2$ at $\tau = \tau_f$, we desire the optimal control u that drives the system (10) from point A to point B of the cartesian plane (Fig. 2) in minimum time τ_f subject to (12). We adopt the notation z_1^P and z_2^P for the path length coordinate z_1 and velocity z_2 of a point P of the prescribed path $R(z_1)$. Thus, we have $z_1^A = z_{10}$, $z_2^A = z_{20}$, $z_1^B = z_{1f}$ and $z_2^B = z_{2f}$. Notice that without loss of generality we may assume that $z_2(\tau) > 0$, $\forall \tau \in (\tau_0, \tau_f)$.

The cost function to be minimized is written as

$$J = \int_{\tau_0}^{\tau_f} \mathrm{d}\sigma. \tag{18}$$

The Hamiltonian for this problem is

$$H(z, \lambda, u) = 1 + \lambda_1 z_2 + \lambda_2 u \sqrt{1 - \left(\frac{z_2^4}{R^2(z_1)} \right)} + \mu C_0(z_1, z_2). \tag{19}$$

The system of adjoint equations is

$$\dot{\lambda}_1 = -\frac{\partial H}{\partial z_1} = -\lambda_2 u \frac{z_2^4}{\sqrt{1 - z_2^4/R^2(z_1)}} \frac{R'(z_1)}{R^3(z_1)} + \mu \operatorname{sgn} R(z_1) R'(z_1), \tag{20}$$

$$\dot{\lambda}_2 = -\frac{\partial H}{\partial z_2} = -\lambda_1 + 2\lambda_2 u \frac{z_2^3}{R^2(z_1)\sqrt{1 - z_2^4/R^2(z_1)}} - 2z_2\mu. \tag{21}$$

The Kuhn-Tucker conditions imply

$$\mu = 0 \text{ for } C_0(z_1, z_2) < 0 \text{ and } \mu \geq 0 \text{ for } C_0(z_1, z_2) = 0. \tag{22}$$

The transversality condition implies $H(\tau_f) = 0$, and since the Hamiltonian does not depend explicitly on time it also follows that

$$H(\tau) = 0, \quad \forall \tau \in [\tau_0, \tau_f]. \tag{23}$$

Consider first the case of an inactive constraint, $C_0(z_1, z_2) < 0$. In this case $\mu = 0$ and Pontryagin's Maximum Principle leads to the optimal control

$$u^* = \operatorname{argmin}_{u \in [-1, +1]} H(z, \lambda, u) = \begin{cases} -1 \text{ for } \lambda_2 > 0, \\ +1 \text{ for } \lambda_2 < 0, \end{cases} \tag{24}$$

which implies,

$$u^*(\tau) = -\operatorname{sgn}\lambda_2(\tau). \tag{25}$$

11

Therefore λ_2 is the switching function, which determines the value of u^*.

Let us consider the possibility of a singular control interval in the optimal solution, i.e., the existence of a time interval $(\tau_1, \tau_2) \subset [\tau_0, \tau_f]$ such that $\lambda_2(\tau) = 0$, for all $\tau \in (\tau_1, \tau_2)$. Equation (20) implies that $\dot{\lambda}_1(\tau) = 0$ for all $\tau \in (\tau_1, \tau_2)$, or equivalently $\lambda_1(\tau) = \lambda_{10} = \text{constant}$ for all $\tau \in (\tau_1, \tau_2)$. Equation (21) implies $\dot{\lambda}_2(\tau) = -\lambda_{10}\tau$ for all $\tau \in (\tau_1, \tau_2)$. In addition, $\lambda_2(\tau) = 0$ and $\dot{\lambda}_2(\tau) = 0$ for all $\tau \in (\tau_1, \tau_2)$, and thus we have $\lambda_{10} = 0$ and $\lambda_1(\tau) = \lambda_2(\tau) = 0$ for all $\tau \in (\tau_1, \tau_2)$. Equation (19) then gives $H(\tau) = 1$ for $\tau \in (\tau_1, \tau_2)$, which contradicts the condition (23) that $H(\tau) = 0$ for all $\tau \in [\tau_0, \tau_f]$.

We have thus proven the following proposition.

Proposition 1 *Assuming that throughout the optimal trajectory $C_0(z_1, z_2) < 0$, there can be no singular subarc.*

This proposition states that to optimally transverse a path in minimum time, the maximum available force must be used at all times and the optimal trajectory is composed only of bang-bang subarcs ($u = +1$ or $u = -1$), assuming that the optimal state trajectory remains inside $\mathcal{S}$.

3.2.3 Solution for Special Cases of Path Curvature: Inactive Constraint

In the following, we provide solutions to the previous minimum-time problem for several special cases of $R(z_1)$. First, we consider the simplest case when the constraint (12) remains inactive. According to Lemma 1 this occurs only if $R'(z_1) \neq 0$. We distinguish two different cases: paths of decreasing curvature and paths of increasing curvature.

3.2.4 Path of Decreasing Curvature

Consider a path of monotonically decreasing curvature from point A to point B in the cartesian plane denoted by

$$\mathcal{P}_{AB}^+ = \left\{ (z_1, R(z_1)) : \ R'(z_1) \, \text{sgn} R(z_1) > 0, \ z_1 \in [z_1^A, z_1^B] \right\}. \tag{26}$$

From Proposition 1 we know that the optimal path is composed solely of subarcs of maximum acceleration or maximum deceleration.

Equation (20) with $R'(z_1) \, \text{sgn} R(z_1) > 0$ yields $\dot{\lambda}_1(\tau) \geq 0$, for all $\tau \in [\tau_0, \tau_f]$. Suppose now that there exists a switching time $\tau_1 \in (\tau_0, \tau_f)$. It follows that $\lambda_2(\tau_1) = 0$. The transversality condition (23) implies $\lambda_1(\tau_1) = -1/z_2(\tau_1)$. For any $\tau \in [\tau_0, \tau_1)$ we have that

$$
\begin{aligned}
-\frac{1}{z_2(\tau)} &\leq \frac{-1 + |\lambda_2|\sqrt{1 - z_2^4/R^2(z_1)}}{z_2(\tau)} = \lambda_1(\tau) \\
&\leq \lambda_1(\tau_1) = -\frac{1}{z_2(\tau_1)}
\end{aligned}
\tag{27}
$$

since λ_1 is non-decreasing. Inequality (27) implies that $z_2(\tau) \leq z_2(\tau_1)$ for all $\tau \in [\tau_0, \tau_1)$, from which we conclude that τ_1 is a switching point from $u = +1$ to $u = -1$.

Following the same steps as for the switching point τ_1, it is easy to prove that any other switching point $\tau_2 \in (\tau_0, \tau_1)$ has to be from $u = +1$ to $u = -1$. Obviously, there can be no consecutive switching points from $u = +1$ to $u = -1$ without a switching from $u = -1$ to $u = +1$ in between. Thus, we rule out the possibility of existence of a second switching point $\tau_2 \in (\tau_0, \tau_1)$. Finally, suppose that there exists a switching point $\tau_3 \in (\tau_1, \tau_f)$. The transversality condition (23) implies $\lambda_1(\tau_3) = -1/z_2(\tau_3)$. Since λ_1 is non-decreasing we have that $\lambda_1(\tau_1) \leq \lambda_1(\tau_3)$ or that

$-1/z_2(\tau_1) \le -1/z_2(\tau_3)$ and finally that $z_2(\tau_1) \le z_2(\tau_3)$, implying that the vehicle accelerates from τ_1 to τ_3, which contradicts the fact that $u(\tau) = -1$ for $\tau \in (\tau_1, \tau_3)$. It follows that we can have only one switching in the control.

Let now $Z_A^+(z_1)$ be the characteristic constructed by forward integration of (10) from (z_1^A, z_2^A) with $u = +1$, and $Z_B^-(z_1)$ be the characteristic constructed by backward integration of (10) from (z_1^B, z_2^B) with $u = -1$. We have therefore the following proposition for the optimal trajectory on paths of monotonically decreasing curvature.

Proposition 2 *In the case of a path of monotonically decreasing curvature $\mathcal{P}_{AB}^+$ there can be at most one switching in the control, from $u = +1$ to $u = -1$. In this case the optimal solution is given by*

$$z_2^*(z_1) = \min\left\{Z_A^+(z_1), Z_B^-(z_1)\right\}. \tag{28}$$

It is easy to prove the optimality of (28) directly, by showing that $z_2^*(z_1)$ in (28) maximizes the velocity pointwise for all $z_1 \in [z_1^A, z_1^B]$.

3.2.5 Path of Increasing Curvature

Consider a path of monotonically increasing curvature from point A to point B denoted in the cartesian plane by

$$\mathcal{P}_{AB}^- = \left\{(z_1, R(z_1)): \ R'(z_1)\,\mathrm{sgn}R(z_1) < 0, \ z_1 \in [z_1^A, z_1^B]\right\}. \tag{29}$$

Similar to the case of a path of decreasing curvature, the optimal path is composed only of subarcs of maximum acceleration or maximum deceleration, assuming that the optimal trajectories remain in the interior of $\mathcal{S}$ (Proposition 1). An analysis similar to the one of Section 3.2.4 can be followed to show that, assuming the trajectories remain in $\mathcal{S}$, there can be at most one switch in the control, from $u = +1$ to $u = -1$. Below we show that the optimal trajectory does indeed remain in $\mathcal{S}$.

As before, let $Z_A^+(z_1)$ be the characteristic constructed by forward integration of (10) from (z_1^A, z_2^A) with $u = +1$, and $Z_B^-(z_1)$ be the characteristic constructed by backward integration of (10) from (z_1^B, z_2^B) with $u = -1$.

Lemma 2 *Assuming $z_2^B \le z_{2\mathrm{crit}}(z_1^B)$, then $Z_B^-(z_1) < z_{2\mathrm{crit}}(z_1)$ for all $z_1 \in [z_1^A, z_1^B)$.*

Proof: The proof involves two steps. First, we construct the locus $\mathcal{M}$ of points in the z_1-z_2 plane having the following property: the slope of any trajectory beginning from any point in $\mathcal{M} \subset \mathcal{S}$ using the control $u = -1$ is less than or equal to the slope of $z_{2\mathrm{crit}}(z_1)$. In the second step we show that for characteristic path starting in $\mathcal{S}\backslash\mathcal{M}$ constructed by backward integration of (10) with $u = -1$ remains in $\mathcal{S}$.

To this end, note that the smallest possible slope in the z_1-z_2 plane of any feasible trajectory is achieved using maximum deceleration ($u = -1$). In particular, we have

$$\dot{z}_2 = u\sqrt{1 - \frac{z_2^4}{R^2(z_1)}} \Rightarrow z_2' = \frac{u}{z_2}\sqrt{1 - \frac{z_2^4}{R^2(z_1)}}, \tag{30}$$

which for $u = -1$ yields

$$z_{2\mathrm{min}}' = -\frac{1}{z_2}\sqrt{1 - \frac{z_2^4}{R^2(z_1)}}. \tag{31}$$

13

On the other hand, the slope of the $z_{2\text{crit}}(z_1)$ characteristic in (17) is

$$z'_{2\text{crit}}(z_1) = \frac{\text{sgn}R(z_1)R'(z_1)}{2\sqrt{|R(z_1)|}} \triangleq \rho(z_1). \tag{32}$$

Using (31) and (32) we may enforce the inequality $z'_{2\text{min}} \leq z'_{2\text{crit}}$ by

$$P(z_2) \triangleq z_2^4 + R^2(z_1)\rho^2(z_1)z_2^2 - R^2(z_1) \leq 0. \tag{33}$$

Solving for z_2^2, the roots of $P(z_2)$ are

$$r_{1,2} \triangleq \frac{-R^2(z_1)\rho^2 \mp \sqrt{R(z_1)^4\rho^4 + 4R^2(z_1)}}{2}, \tag{34}$$

and for (33) to hold, given $z_2 > 0$, we must have

$$z_2 \leq \sqrt{r_2} = \left(\frac{-R^2(z_1)\rho^2(z_1) + \sqrt{R^4(z_1)\rho^4(z_1) + 4R^2(z_1)}}{2} \right)^{1/2}. \tag{35}$$

In the limiting case, when $z'_{2\text{min}} = z'_{2\text{crit}}$, we have $z_{2\text{safe}} = \sqrt{r_2}$. An explicit relationship between $z_{2\text{safe}}$ and $z_{2\text{crit}}$ is given by the equation

$$z_{2\text{safe}}^4 - z_{2\text{crit}}^4 + \left(\frac{R'(z_1)^2}{4} \right) z_{2\text{safe}}^2 z_{2\text{crit}}^2 = 0, \tag{36}$$

which implies that $z_{2\text{safe}}(z_1) < z_{2\text{crit}}(z_1)$ for all $z_1 \in [z_1^A, z_2^B]$. The set $\mathcal{M}$ is therefore the area underneath the curve $z_{2\text{safe}}(z_1)$. It follows that $\mathcal{M} \subset \mathcal{S}$. The $z_{2\text{crit}}(z_1)$ and $z_{2\text{safe}}(z_1)$ curves for paths of increasing curvature are shown in Fig. 3.

To finish the proof, notice that for any trajectory starting in $\mathcal{S}\backslash\mathcal{M}$ (the area between the characteristics $z_{2\text{safe}}(z_1)$ and $z_{2\text{crit}}(z_1)$ in Fig. 3) using $u = -1$, we have that $z'_{2\text{min}} > z'_{2\text{crit}}$. Integrating now backwards in time from z_1^B to z_1 ($dz_1 < 0$) using $u = -1$ one obtains

$$\int_{z_1^B}^{z_1} dz_{2\text{min}} < \int_{z_1^B}^{z_1} dz_{2\text{crit}}, \tag{37}$$

or $z_{2\text{min}}(z_1) - z_{2\text{min}}(z_1^B) < z_{2\text{crit}}(z_1) - z_{2\text{crit}}(z_1^B)$. Since $z_{2\text{min}}(z_1^B) \leq z_{2\text{crit}}(z_1^B)$ for points in $\mathcal{S}\backslash\mathcal{M}$ it follows that $z_{2\text{min}}(z_1) < z_{2\text{crit}}(z_1)$. See also Fig. 4.

We conclude that for an increasing curvature path $\mathcal{P}_{AB}^-$,

$$Z_B^-(z_1) < z_{2\text{crit}}(z_1), \quad z_1 \in [z_1^A, z_1^B), \tag{38}$$

given that $z_2^B \leq z_{2\text{crit}}(z_1^B)$. ∎

Lemma 2 implies, in particular, that

$$z_2(z_1) = \min\left\{ Z_A^+(z_1), Z_B^-(z_1) \right\} < z_{2\text{crit}}(z_1), \quad z_1 \in [z_1^A, z_1^B). \tag{39}$$

Hence the constraint (12) remains inactive throughout the optimal trajectory. We have therefore shown the following result for the optimal trajectory on paths of monotonically increasing curvature.

Proposition 3 *In the case of a path of monotonically decreasing curvature $\mathcal{P}_{AB}^-$, there can be at most one switching in the control, from $u = +1$ to $u = -1$. In this case the optimal solution is given by*

$$z_2^*(z_1) = \min\left\{ Z_A^+(z_1), Z_B^-(z_1) \right\}. \tag{40}$$
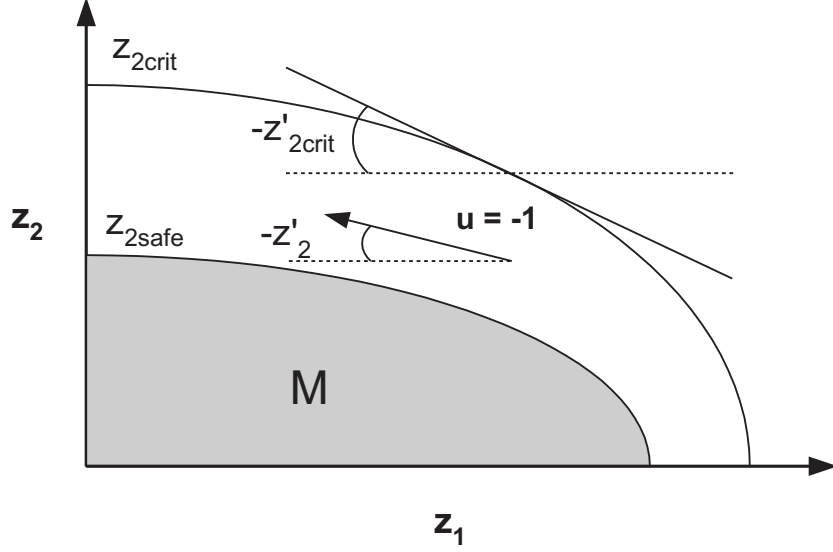
14

Figure 3: In the area between $z_{2\text{crit}}$ and $z_{2\text{safe}}$ we can integrate backward in time with $u = -1$ without intersecting $z_{2\text{crit}}$.

3.2.6 Numerical Example

Consider a path of increasing magnitude of the radius (decreasing curvature) from point A to point B as in Fig. 5(a), described by the following equation

$$R(z_1) = -0.5z_1 - 10. \tag{41}$$

Assume that the vehicle starts from point A with zero velocity and reaches point B with zero velocity as well. The switching point SP is determined by the intersection of the characteristic $Z_A^+(z_1)$ in Fig. 5(b), created by forward integration of the equations of motion (10) with initial conditions (z_1^A, z_2^A) using $u = +1$, with the characteristic $Z_B^-(z_1)$, created by backward integration of the equations of motion with initial conditions (z_1^B, z_2^B) using $u = -1$. Equivalently, the optimal solution $z_2^*(z_1)$ is given by

$$z_2^*(z_1) = \min \left\{ Z_A^+(z_1), Z_B^-(z_1) \right\}. \tag{42}$$

Figure 6 confirms that the optimality conditions hold, i.e. the switching function λ_2 changes sign at the switching point of the control input.

3.2.7 Solution for Special Cases of Path Curvature: Active Constraint

In this section we consider the case when the constraint (12) is active, i.e., $C_0(z_1, z_2) = 0$. First, observe that when the speed of the vehicle takes the critical value (17), equation (12) implies that $(z_1, z_2) \in \partial S$. In this case $f_n = F_{\max}$ and $\dot{z}_2 = 0$ from (10). The control input u cannot affect the value of the velocity and loss of controllability ensues. This may also be interpreted as a loss of the ability to generate tangential force f_t, since the whole force capacity $F_{\max}$ is used to produce the required centripetal force f_n. From Lemma 1 it follows that this case is possible only for paths of constant curvature. In the remaining of this section we will therefore consider only paths with $R'(z_1) = 0$.
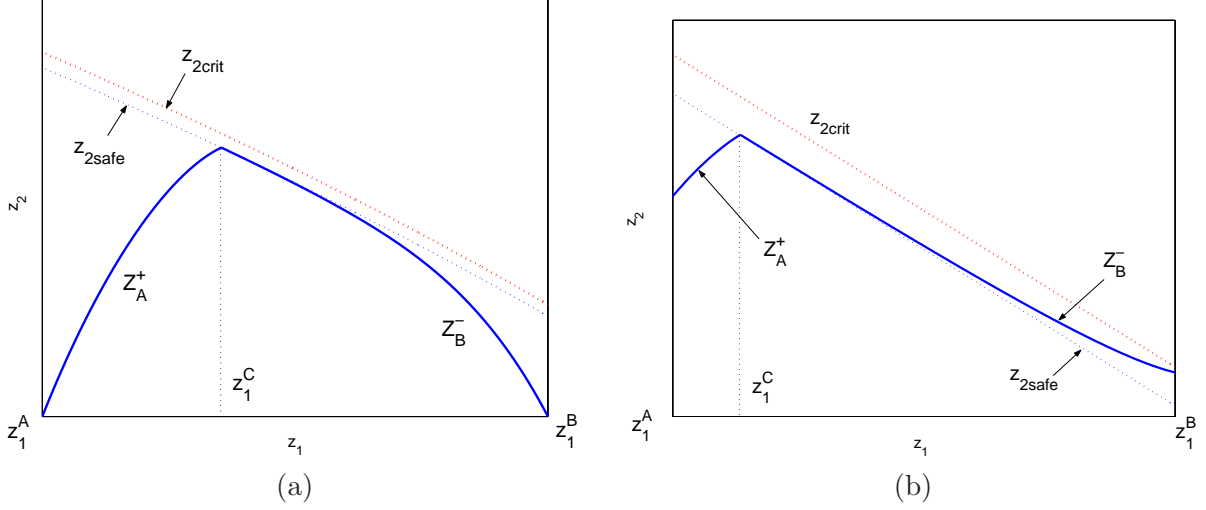
15

Figure 4: Optimal solution for a path of decreasing curvature near the state constraint.

In order to avoid the difficulty arising from the loss of controllability for the case of a path of constant curvature, we introduce the constraint

$$C_\epsilon(z_1, z_2) \triangleq z_2^2 + \epsilon - |R(z_1)| = 0, \tag{43}$$

where $\epsilon > 0$ is a small positive scalar. We investigate optimal paths that satisfy this constraint and the we take $\epsilon \to 0$ to recover the case of $C_0(z_1, z_2) = 0$ at the limit.

An easy calculation shows that the control law that keeps the vehicle on the constraint (43) is given by

$$u_{\text{sc}} = \frac{R(z_1)R'(z_1)}{2\sqrt{2|R(z_1)|\epsilon - \epsilon^2}}, \tag{44}$$

which, upon $R'(z_1) = 0$ yields $u_{\text{sc}} \equiv 0$ for any $\epsilon > 0$. Hence $\lim_{\epsilon \to 0} u_{\text{sc}} = 0$.

Consider now a path of constant curvature $\mathcal{P}_{AF}^0$. Figure 7 shows the characteristic $Z_A^+(z_1)$ constructed by forward integration of (10) from (z_1^A, z_2^A) with $u = +1$, the characteristic $Z_{AF}^0(z_1)$ given by $z_2(z_1) = \sqrt{|R(z_1)| - \epsilon} < z_{2\text{crit}}(z_1)$, for $z_1 \in [z_1^A, z_1^F]$, with $\epsilon > 0$, and the characteristic $Z_F^-(z_1)$ constructed by backward integration of (10) from (z_1^F, z_2^F) with $u = -1$. Notice that the characteristic $Z_{AF}^0(z_1)$ is constructed with $u = 0$, which coincides with u_{sc} in (44) for $R'(z_1) = 0$. On the characteristic $Z_{AF}^0(z_1)$ the constraint (43) remains active, i.e., $C_\epsilon(z_1, Z_{AF}^0(z_1)) = 0$.

Proposition 4 *In the case of a path of constant curvature $\mathcal{P}_{AF}^0$, assuming $\epsilon > 0$, the optimal solution is given by*

$$z_2^*(z_1) = \min\left\{Z_A^+(z_1), Z_{AF}^0(z_1), Z_F^-(z_1)\right\}. \tag{45}$$

The trajectory from z_1^A to z_1^B in Fig. 7 maximizes point-wise the velocity since it is constructed using maximum acceleration $u = +1$ from a fixed initial velocity $z_2(\tau_0) = z_2^A$. The velocity of the trajectory from z_1^B to z_1^E is equal to the maximum allowable value, $\sqrt{|R(z_1)| - \epsilon}$. Finally, the trajectory from z_1^E to z_1^F on Z_F^- is also of maximum point-wise velocity, since Z_F^- is constructed using maximum acceleration $u = -1$ backward in time starting from a fixed initial velocity $z_2(\tau_f) = z_2^F$. Thus, the overall trajectory of (45) maximizes the velocity point-wise, which proves the optimality of the proposed solution.
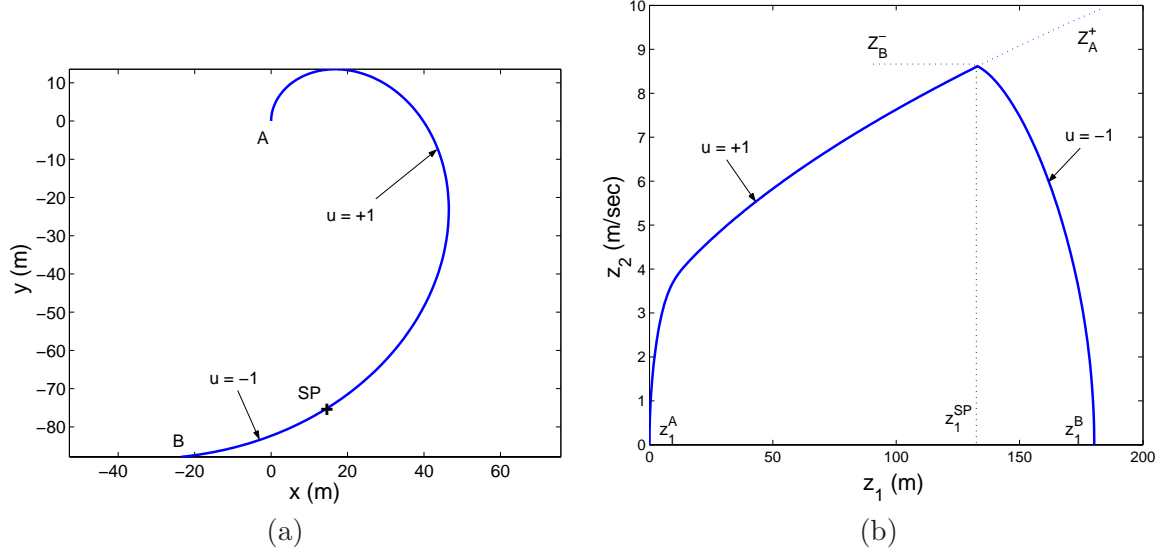
16

Figure 5: Optimal velocity profile through a path of increasing radius.

Let now $\epsilon \to 0$ and assume that at some point $\tau_c \in (\tau_0, \tau_f)$ we have $z_2(\tau_c) = z_{2\text{crit}}(z_1(\tau_c))$, as in (17). This point corresponds to $(z_1^C, z_{2\text{crit}})$ in Fig. 7. Since the square root in equation (10) becomes zero, the tangential acceleration becomes zero and hence $\dot{z}_2(\tau_c) = 0$. Since we are on a path of constant curvature, $z_2(\tau) = z_{2\text{crit}}(z_1(\tau))$ for all $\tau \geq \tau_c$ and thus once controllability is lost, it cannot be regained. This means that when the vehicle operates at $(z_1^D, z_{2\text{crit}})$, it cannot switch to $Z_B^-(z_1)$ and the vehicle continues to travel with $z_{2\text{crit}}$. We conclude that in case of a path of constant curvature $\mathcal{P}_{AF}^0$, unless the final velocity $z_2^F = z_{2\text{crit}}(z_1^F)$ we cannot allow $\epsilon = 0$. We have therefore shown the following corollary.

Corollary 2 *Consider the minimum-time problem (10), and assume a path of constant curvature, $R(z_1) = c$. If $z_2(\tau_f) \neq \sqrt{|c|}$ an optimal solution does not exist.*

In the sequel we investigate paths composed of concatenations of paths investigated thus far. Such concatenations will allow us to construct the optimal trajectories, along with the corresponding optimal controls, by piecing together the solutions provided by Propositions 1-4.

3.2.8 Path with $\min R(z_1)$

Consider now a path of increasing curvature $\mathcal{P}_{AC}^-$ followed by a path of decreasing curvature $\mathcal{P}_{CB}^+$ as in Fig. 8. We adopt the following notation for the path from point A to point B

$$\mathcal{P}_{ACB}^{\mp} = \mathcal{P}_{AC}^- \circ \mathcal{P}_{CB}^+ = \left\{ (z_1, R(z_1)) : R'(z_1) \operatorname{sgn} R(z_1) < 0, \ z_1 \in [z_1^A, z_1^C), \right.$$
$$\left. R'(z_1) \operatorname{sgn} R(z_1) > 0, \ z_1 \in [z_1^C, z_1^B]) \right\}, \tag{46}$$

where "$\circ$" denotes the concatenation operator. The function $R(z_1)$ has a minimum at z_1^C (see Fig. 8).

Let $z_2^*(z_1)$ denote the minimum time solution from A to B and z_2^{C*} denote the velocity at point C of the $z_2^*(z_1)$ trajectory. According to Bellman's Principle of Optimality if the solution $A \to B$ is optimal then the first part of this solution, $A \to C$, solves the minimum time problem from A to C with the final condition $z_2(\tau_f) = z_2^{C*}$. Similarly, the second part, $C \to B$, solves the minimum-time problem from C to B with initial condition $z_2(\tau_0) = z_2^{C*}$.
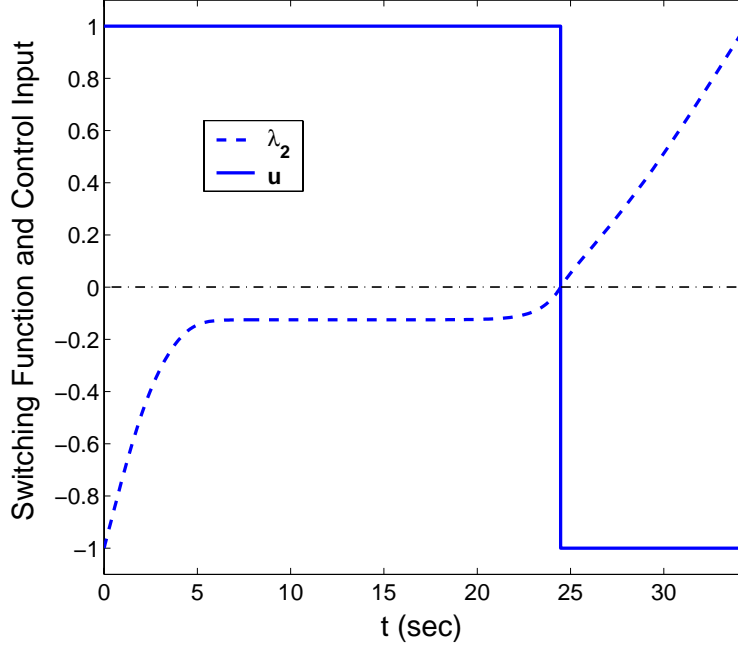
17

Figure 6: Switching function and control input time history for the path shown in Fig. 5(a).

The velocity z_2^{C*} is not known a priori however, and the solution $A \to B$ cannot be constructed from the solutions $A \to C$ and $C \to B$. Nonetheless, we do know the allowable switchings of the control for the subarcs $A \to C$ and $C \to B$ from the analysis in Sections 3.2.4 and 3.2.5.

On the part $A \to C$ we have a path of increasing radius, and according to Section 3.2.4 the possible optimal velocity profiles, summarized in Fig. 9(a), are: $u = +1$ (Case 1), $u = -1$ (Case 2) or $u = +1$ that switches once to $u = -1$ (Case 3). Similarly, on the part $C \to B$ we have a path of decreasing radius and according to Section 3.2.5 the possible optimal velocity profiles, summarized in Fig. 9(b), are: $u = +1$ (Case a), $u = -1$ (Case b) or $u = +1$ that switches once to $u = -1$ (Case c). For Bellman's Principle of Optimality to hold, the overall solution from A to B will consist of the subarcs $A \to C$ and $C \to B$ that correspond to Cases 1,2,3 and Cases a,b,c (Fig 9), respectively. Thus, all the possible optimal velocity profiles for the overall problem from A to B are all the possible combinations of Cases 1,2,3 and Cases a,b,c. These are shown in Fig 10. In the following, we discuss each case separately in order to compute the optimal velocity at point C.

Case 1a corresponds to $u = +1$ in both subarcs, $A \to C$ and $C \to B$ and the optimal solution $z_2^*(z_1)$ coincides with the characteristic $Z_A^+(z_1)$. Obviously, there is no other path that satisfies the boundary conditions at points A and B. The velocity at point C has to be less than or equal to $z_{2\text{crit}}(z_1^C)$. In this case the optimal velocity z_2^{C*} is determined by the boundary conditions at A and B.

Case 1b corresponds to $u = +1$ from $A \to C$ and $u = -1$ from $C \to B$. Contrary to the previous case, it is now possible to satisfy the boundary conditions at A and B using acceptable control switchings. Consider, for example, the solution using the sequence of characteristics Z_A^+ ($u = +1$), Z_m ($u = -1$), Z_n ($u = +1$), Z_B^- ($u = -1$) shown in Fig. 10, Case 1b. However, it is obvious that the solution using one switching from Z_A^+ to Z_B^- maximizes velocity point-wise between A and B (for the given boundary conditions), and thus this is the optimal solution. Again, the velocity at point C has to be less than or equal to $z_{2\text{crit}}(z_1^C)$.

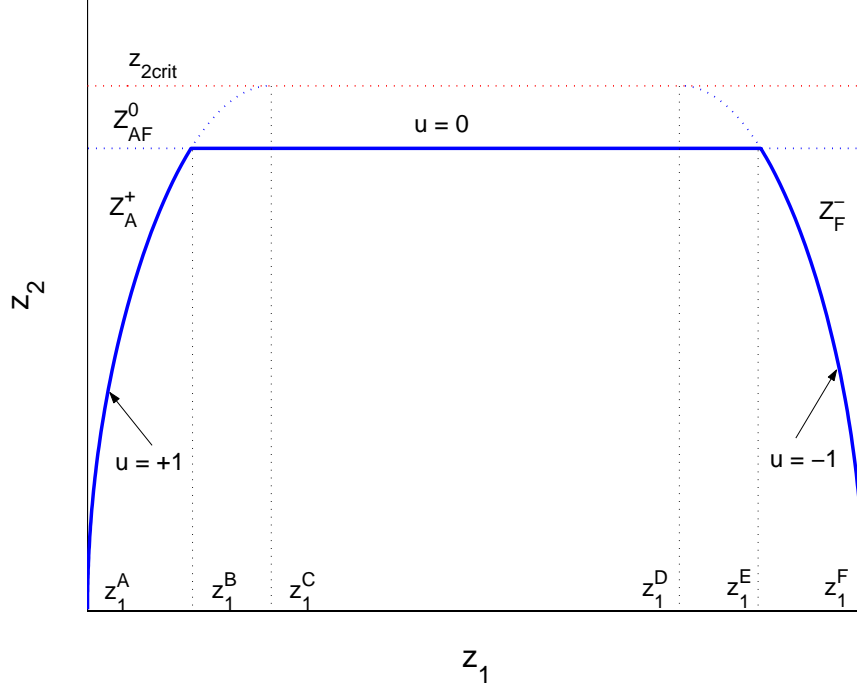**Case 1c** corresponds to $u = +1$ from $A \to C$ and switching of the control from $u = +1$ to

18

Figure 7: Constant radius path; active constraint case.

$u = -1$ along the subarc $C \to B$. This case is similar to the Case 1b. The overall trajectory consists of one switching from acceleration to deceleration. However, this time the switching does not take place at point C due to the different boundary conditions at A and B. Again, the velocity at point C has to be less than or equal to the critical one.

Case 2a corresponds to $u = -1$ from $A \to C$ and $u = +1$ from $C \to B$. Assume, as shown in Case 2a of Fig. 10, that there are other solutions that consist of admissible switchings, and which satisfy the same boundary conditions at points A and B. In fact, the solution that corresponds to Case 2a, constructed by the characteristic paths Z_C^- and Z_C^+, is the one with the lowest velocity point-wise between A and B. We conclude that Case 2a will be optimal only if $z_2^{C*} = z_{2\mathrm{crit}}(z_1^C)$, which is acceptable since a path of decreasing curvature follows after point C and controllability is regained immediately.

Case 2b corresponds to $u = -1$ in both subarcs, $A \to C$ and $C \to B$. It is completely equivalent to Case 1a if we reverse the boundary conditions at the points A and B.

Case 2c corresponds to $u = -1$ from $A \to C$ and one switching from $u = +1$ to $u = -1$ in the subarc from $C \to B$. As in Case 2a, unless $z_2^{C*} = z_{2\mathrm{crit}}(z_1^C)$ there are other solutions that satisfy the boundary conditions at points A and B consisting of higher velocities at all points between A and B.

Case 3a corresponds to one switching from $u = +1$ to $u = -1$ along the subarc $A \to C$ and to $u = +1$ along $C \to B$. This case is equivalent to the Case 2c if we switch the boundary conditions of points A and B.

Case 3b corresponds to one switching from $u = +1$ to $u = -1$ along the subarc $A \to C$ and to $u = -1$ from $C \to B$. It is equivalent to Cases 1b and 1c; however, in this case the switching of control occurs before point C.

Case 3c corresponds to one switching from $u = +1$ to $u = -1$ along the subarc $A \to C$ and switching from $u = +1$ to $u = -1$ along the subarc $C \to B$. Unless $z_2^{C*} = z_{2\mathrm{crit}}(z_1^C)$ there are
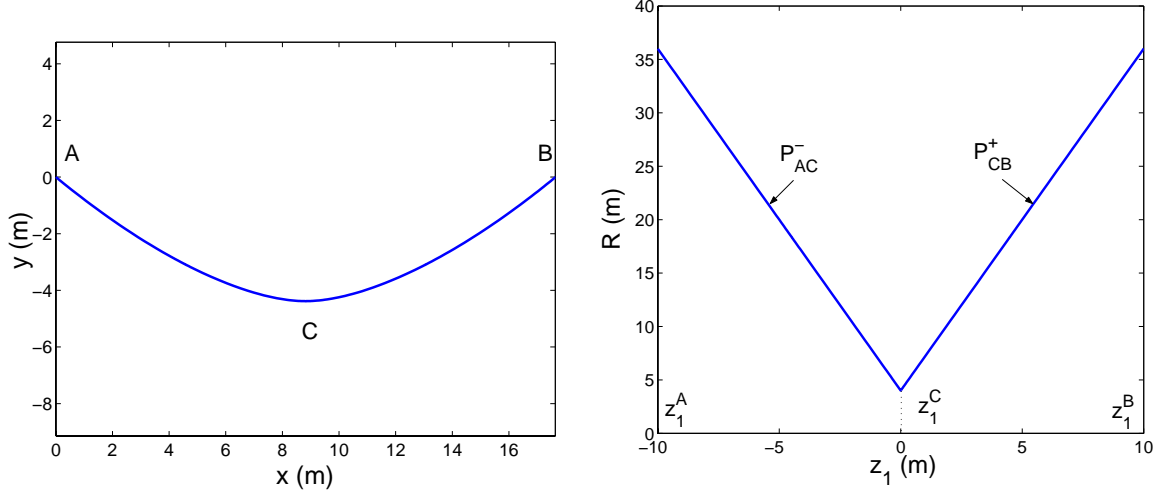
19

Figure 8: Path with minimum radius at point C, in cartesian coordinates (left); path radius as a function of path length (right).

other solutions that satisfy the boundary conditions at points A and B, which all consist of higher velocity at all points.

From the previous analysis we conclude that there are only two possible scenarios for the value of z_2^{C*}. In Cases 1a, 2a, 3a, 2b and 3b we have $z_2^{C*} \leq z_{2\mathrm{crit}}(z_1^C)$ and z_{2C}^* is determined by satisfying the boundary conditions of A and B using allowable control switches. In Cases 2a, 2c, 3a and 3c we have $z_2^{C*} = z_{2\mathrm{crit}}(z_1^C)$ and a control switch from $u = -1$ to $u = +1$ at C.

Next, we propose a methodology to construct the overall optimal solution for a path with curvature switching from increasing to decreasing at a point C. Starting from (z_1^A, z_2^A) we construct the characteristic $Z_A^+(z_1)$ integrating the equations of motion (10) forward in time using $u = +1$. Starting from (z_1^B, z_2^B) we construct the characteristic $Z_B^-(z_1)$ integrating the equations of motion (10) backward in time using $u = -1$. Starting from $(z_1^C, z_{2\mathrm{crit}}(z_1^C))$ we construct the characteristic $Z_C^-(z_1)$ integrating the equations of motion (10) backward in time using $u = -1$. Finally, starting from $(z_1^C, z_{2\mathrm{crit}}(z_1^C))$ we construct the characteristic $Z_C^+(z_1)$ integrating the equations of motion (10) forward in time using $u = +1$. The optimal velocity profile is then given by

$$z_2^*(z_1) \quad = \quad \min \left\{ Z_A^+(z_1), Z_C^-(z_1), Z_C^+(z_1), Z_B^-(z_1) \right\}. \tag{47}$$

It is easy to show that (47) reproduces all the cases of Fig. 10.

3.2.9 Path with $\max R(z_1)$

Consider now a path of decreasing curvature $\mathcal{P}_{AC}^+$ followed by a path of increasing curvature $\mathcal{P}_{CB}^-$. We adopt the following notation for the path from point A to point B

$$\mathcal{P}_{ACB}^\pm = \mathcal{P}_{AC}^+ \circ \mathcal{P}_{CB}^-. \tag{48}$$

Clearly, in this case the function $R(z_1)$ has a maximum at z_1^C. All possible scenarios that may appear along the subarcs $A \to C$ and $C \to B$ according to the solutions presented in Sections 3.2.4 and 3.2.5 may be summarized in accordance to Fig. 9.

In Section 3.2.8 we concluded that Cases 2a, 2c, 3a and 3c may appear as the optimal solutions only if the velocity at C is $z_2^{C*} = z_{2\mathrm{crit}}(z_1^C)$. Since C is a point of maximum radius, the critical
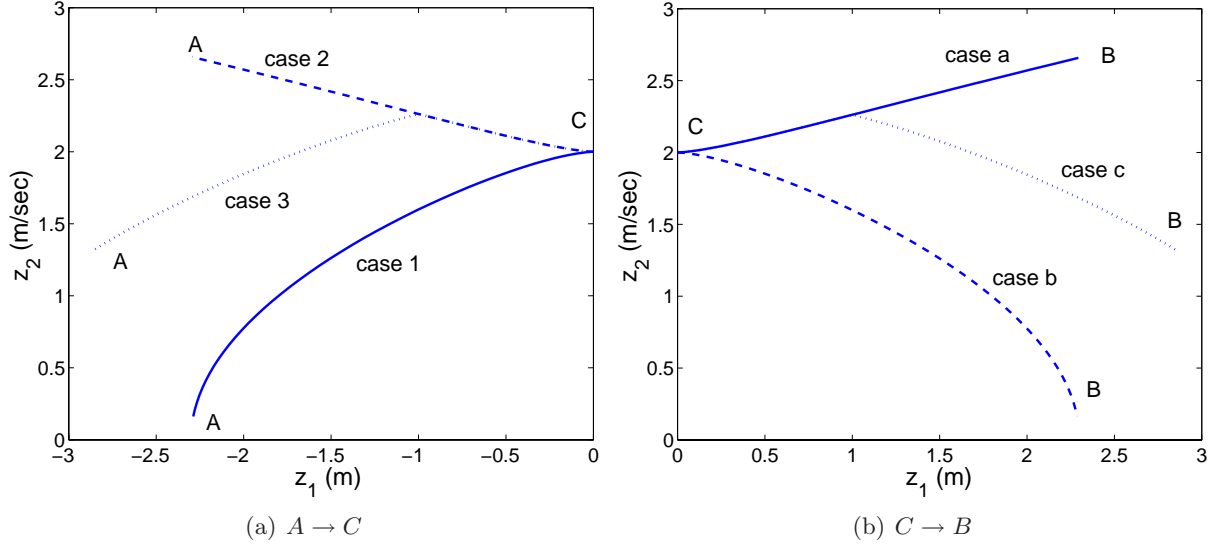
20

Figure 9: Possible optimal velocity profiles before (left) and after (right) point C.

velocity at point C is larger compared to any other point from A to B. That is,

$$z_{2\text{crit}}(z_1) < z_{2\text{crit}}(z_1^C) \quad \text{for} \quad z_1 \in [z_1^A, z_1^C) \cup (z_1^C, z_1^B]. \tag{49}$$

On the other hand, in Cases 2a, 2c, 3a and 3c the velocity at point C is a local minimum. That is, there exists $\delta > 0$ such that $z_2^{C*} < z_2(z_1)$ for $z_1 \in (z_1^C - \delta, z_1^C + \delta)$. For $z_2^{C*} = z_{2\text{crit}}(z_1^C)$ equation (49) implies that $z_2(z_1) > z_{2\text{crit}}(z_1)$, for all $z_1 \in (z_1^C - \delta, z_1^C + \delta)$, and the vehicle cannot follow the prescribed path. We conclude that Cases 2a, 2c, 3a and 3c cannot appear as optimal solutions in the case of a path with a point C of maximum radius.

The only possible scenarios are Cases 1a, 1b, 1c, 2b and 3b, where the optimal velocity at C is determined by the initial and final boundary conditions. The optimal solution is finally given by

$$z_2^*(z_1) \quad = \quad \min\left\{Z_A^+(z_1), Z_B^-(z_1)\right\}. \tag{50}$$

3.2.10 General Solution

Assume that the given path from point A to point B is composed of a finite number of segments of constant curvature, of segments of monotonically increasing curvature and segments of monotonically decreasing curvature. Let the total number of segments be $n + 1$. The path from point A to point B can then be expressed as

$$\mathcal{P}_{AB} = \mathcal{P}_{AP_1}^{i_1} \circ \mathcal{P}_{P_1 P_2}^{i_2} \circ \mathcal{P}_{P_2 P_3}^{i_3} \circ \cdots \circ \mathcal{P}_{P_n B}^{i_{n+1}}, \tag{51}$$

where $i_k \in \{+, -, 0\}$, $k = 1, 2, ..., n+1$. Let $\mathcal{I}^{\mp}$ denote the set of indices corresponding to points of minimum radius of the path $\mathcal{P}_{AB}$, that is, $\mathcal{I}^{\mp} = \{j : i_j = -, \ i_{j+1} = +\}$, $\mathcal{I}^0$ denote the set of indexes corresponding to the first point of a segment of constant curvature, i.e. $\mathcal{I}^0 = \{j : i_j = 0, \ i_{j-1} \neq 0\}$.

The following algorithm provides an ϵ-suboptimal velocity profile for minimum time travel along the path $\mathcal{P}_{AB}$.
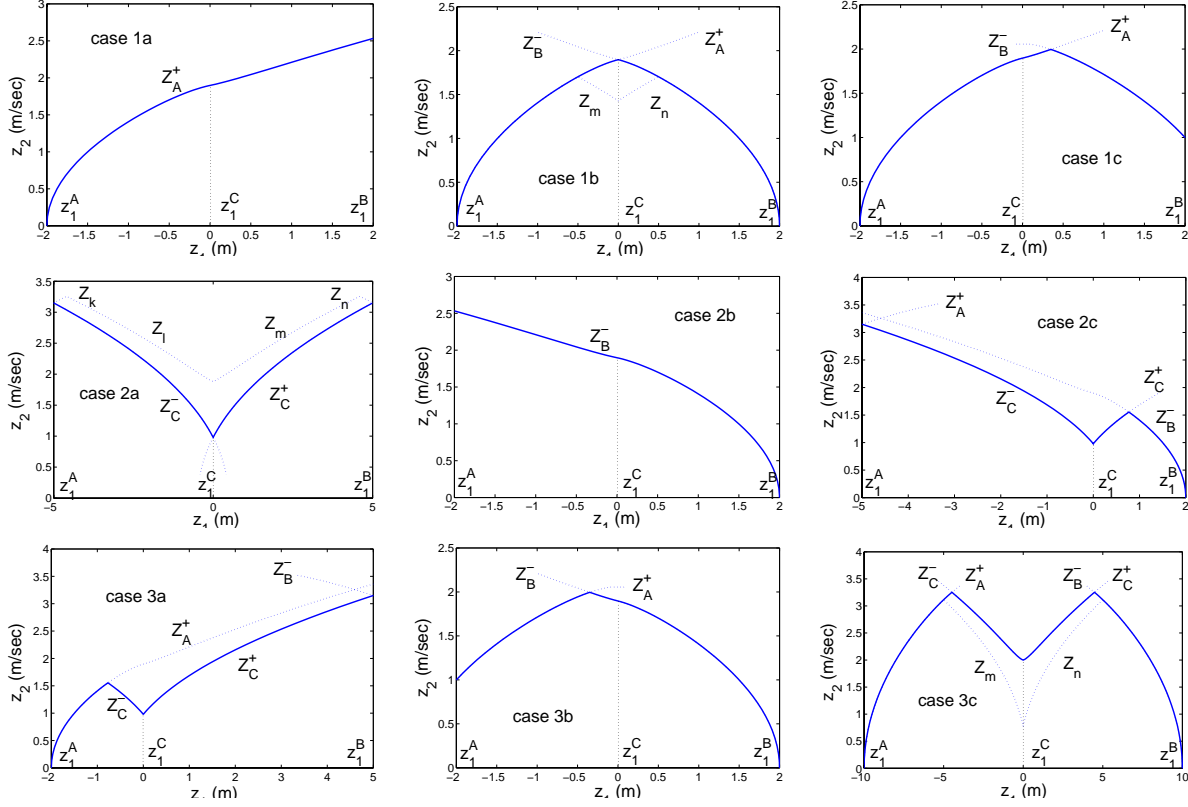
21

Figure 10: All possible optimal velocity profiles from A to B.

ALGORITHM FOR OPTIMAL VELOCITY PROFILE

- From (z_1^A, z_2^A) integrate the equations of motion (10) forward in time with $u = +1$ to construct the characteristic $Z_A^+(z_1)$.

- From (z_1^B, z_2^B) integrate the equations of motion (10) backward in time with $u = -1$ to construct the characteristic $Z_B^-(z_1)$.

- For each point of minimum radius P_k, $k \in \mathcal{I}^{\mp}$, construct the following characteristics: the characteristic $Z_{P_k}^-(z_1)$ by integrating (10) backward in time from $(z_1^{P_k}, z_{2\text{crit}}(z_1^{P_k}))$ using $u = -1$, and the characteristic $Z_{P_k}^+(z_1)$ by integrating (10) forward in time from $(z_1^{P_k}, z_{2\text{crit}}(z_1^{P_k}))$ using $u = +1$.

- For each segment $\mathcal{P}_{P_\ell P_{\ell+1}}^0$ of constant radius $R(z_1) = R_\ell$ where $\ell \in \mathcal{I}^0$, construct the following characteristics: the characteristic $Z_{P_\ell P_{\ell+1}}^0(z_1)$ of constant velocity equal to $\sqrt{|R_\ell| - \epsilon}$, for some $\epsilon > 0$, the characteristic $Z_{P_\ell}^-(z_1)$ by integrating backward in time from $(z_1^{P_\ell}, \sqrt{|R_\ell| - \epsilon})$ using $u = -1$, and the characteristic $Z_{P_{\ell+1}}^+(z_1)$ by integrating forward in time from $(z_1^{P_{\ell+1}}, \sqrt{|R_\ell| - \epsilon})$ using $u = +1$.

- The solution to the minimum time problem is given by

$$z_2^*(z_1) = \min\left\{ Z_A^+(z_1), Z_B^-(z_1), Z_{P_k}^-(z_1), Z_{P_k}^+(z_1), Z_{P_\ell P_{\ell+1}}^0(z_1), Z_{P_\ell}^-(z_1), Z_{P_{\ell+1}}^+(z_1) \right\},$$
(52)

where $k \in \mathcal{I}^{\mp}$ and $\ell \in \mathcal{I}^0$.

22

The previous algorithm will give the optimal velocity profile in case $\mathcal{I}^0 = \varnothing$. Otherwise, and in light of Corollary 2, the solution is suboptimal in the sense that it can always be improved by taking $\epsilon \to 0$ but not zero. Proof of optimality can be easily provided by showing that this solution maximizes the velocity pointwise. We demonstrate this fact in the following example.

3.2.11 Example (General Solution)

Consider the path $\mathcal{P}_{AB}$ shown in Fig. 11(a). We can identify points of minimum radius at P_1, P_4 and P_9 ($\mathcal{I}^{\pm} = \{1, 4, 9\}$), and intervals of constant radius $\mathcal{P}_{P_5 P_6}$ and $\mathcal{P}_{P_7 P_8}$ ($\mathcal{I}^0 = \{5, 7\}$). Figure 11(b) shows the construction of the necessary characteristics using the rules of the previous section. The minimum time solution is given by (52) and it is shown in Fig. 12(a).
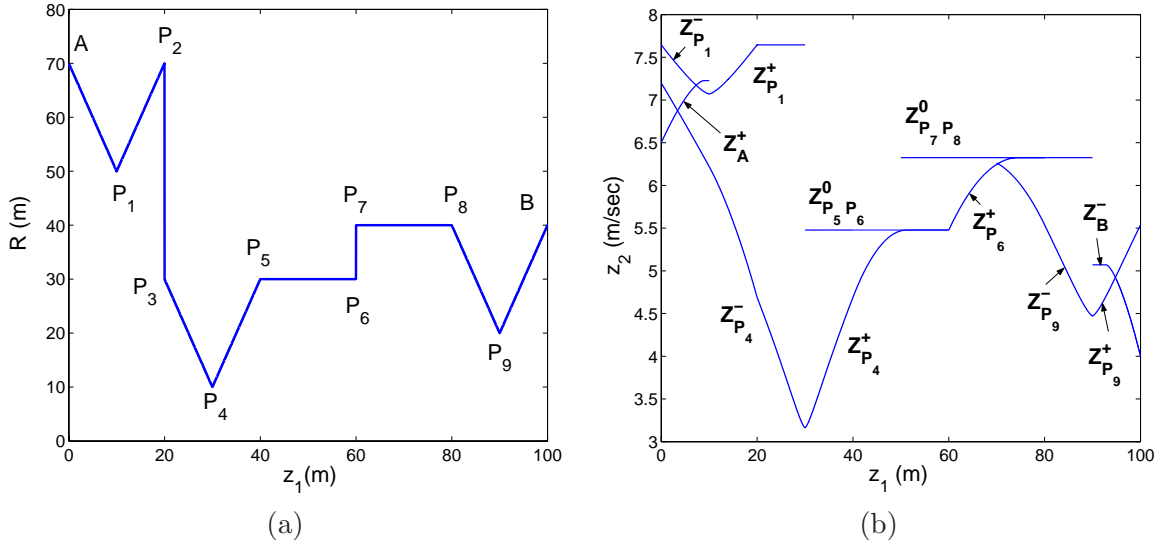

Figure 11: (a) A general case radius profile path; (b) the free boundary conditions problem solutions for constant radius and $\min R$ subarcs.

Consider now the intervals (i) - (viii) along the optimal solution as in Fig. 12(b). In the interval (i) we use maximum acceleration $u = +1$ from the starting point A and thus the velocity is maximized point-wise in the interval (i). In (ii) the vehicle decelerates with $u = -1$ towards the critical velocity at P_4. A trajectory passing from a point of higher velocity in (ii) would violate the constraint (43) at P_4. After P_4 we have maximum acceleration and thus point-wise maximum velocity in (iii). The velocity in (iv) is equal to the maximum allowable from (43). In (v) we have maximum acceleration and thus maximum velocity as in (iii). Point-wise maximality of the velocity in (vi) and (vii) is shown in accordance to (ii) and (iii) respectively. Considering the problem from B to A, the trajectory in (viii) corresponds to maximum acceleration from the fixed condition at B and thus it maximizes the velocity point-wise.

We conclude that the velocity is maximized point-wise throughout the trajectory from A to B, and thus the trajectory computed using (52) is the solution to the minimum time problem.

3.2.12 Application to an F1 circuit

In this section we validate the proposed methodology by applying it to an actual road track. Specifically, we use the previous methodology in order to generate the optimal velocity profile over
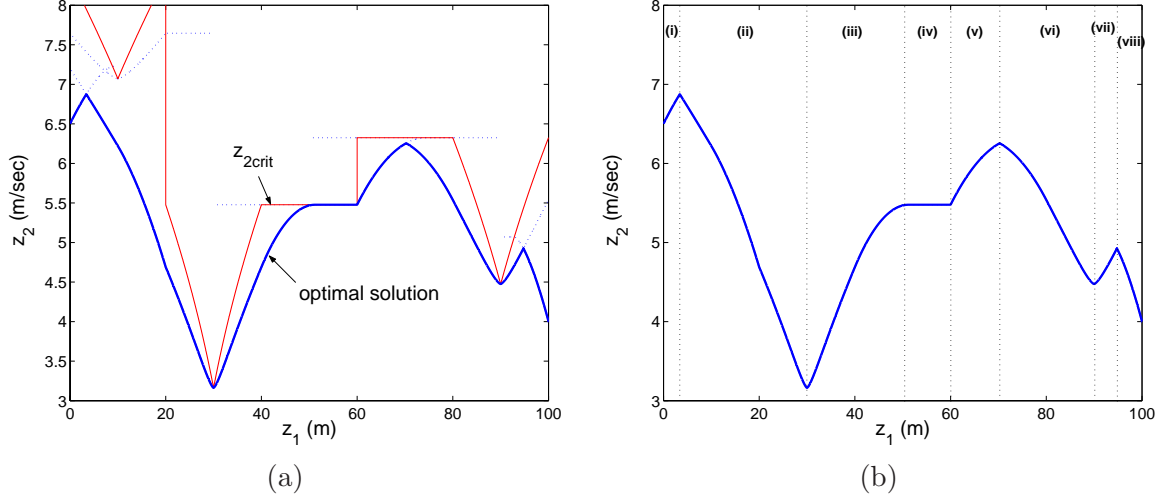
23

Figure 12: Optimal velocity profile for the general case path of Fig. 11.

a F1 circuit, given the acceleration limits of a typical F1 race car. The results are compared to the velocity profiles and lap times achieved by expert F1 race drivers.

Figure 13(a), taken from [17], shows the cartesian coordinates of the Silverstone F1 circuit. The data of Fig. 13(a) were used to generate the curvature profile of this trajectory, which is shown in Fig. 13(b). By matching the performance characteristics of the vehicles in [2], [17] we can
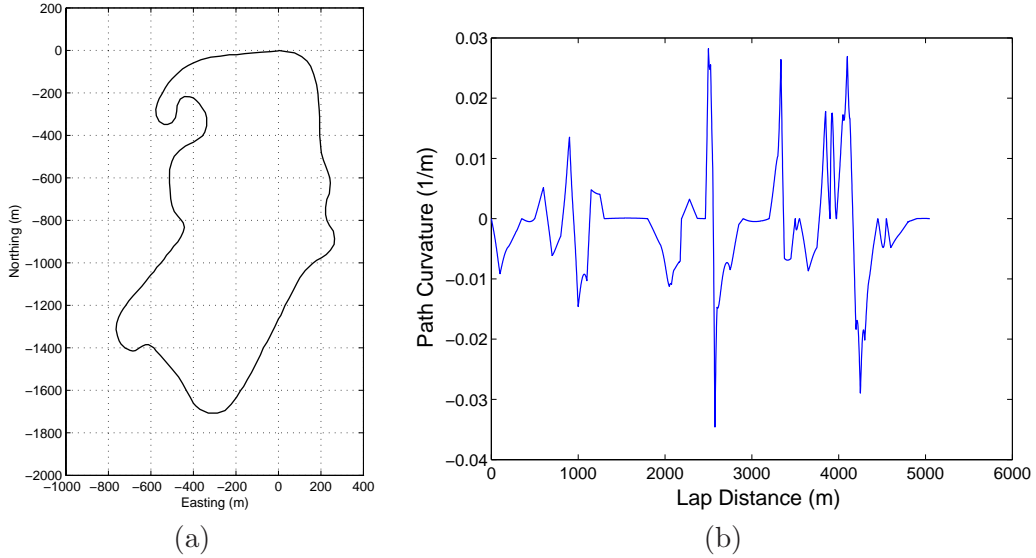

Figure 13: A trajectory followed by an F1 race car in the Silverstone F1 circuit [17] and its curvature profile.

approximate the acceleration limits of a typical F1 race car as follows

$$f_t^{\max}/m = \begin{cases} +16 - 0.0021v^2 \text{ m/sec}^2 \text{ for } u = +1, \\ -18 - 0.0021v^2 \text{ m/sec}^2 \text{ for } u = -1, \end{cases}$$

and

$$f_n^{\max}/m = 30 \text{ m/sec}^2.$$

24

The optimal velocity profile along the trajectory of Fig. 13 is calculated using the methodology of Section 3.2.10. The results are shown in Fig. 14(b). Figure 14(a), taken from [17], shows the velocity measurements for three laps of an F1 car along the Silverstone circuit. The optimally calculated lap time using the proposed approach is 82.7 sec. The measured lap times corresponding to the data of Fig. 14(a) are 86.063 sec, 90.891 sec and 85.805 sec respectively for each lap. Note that the record time for the Silverstone circuit belongs to K. Raikkonen (78.233 sec, McLaren Mercedes, 2004).
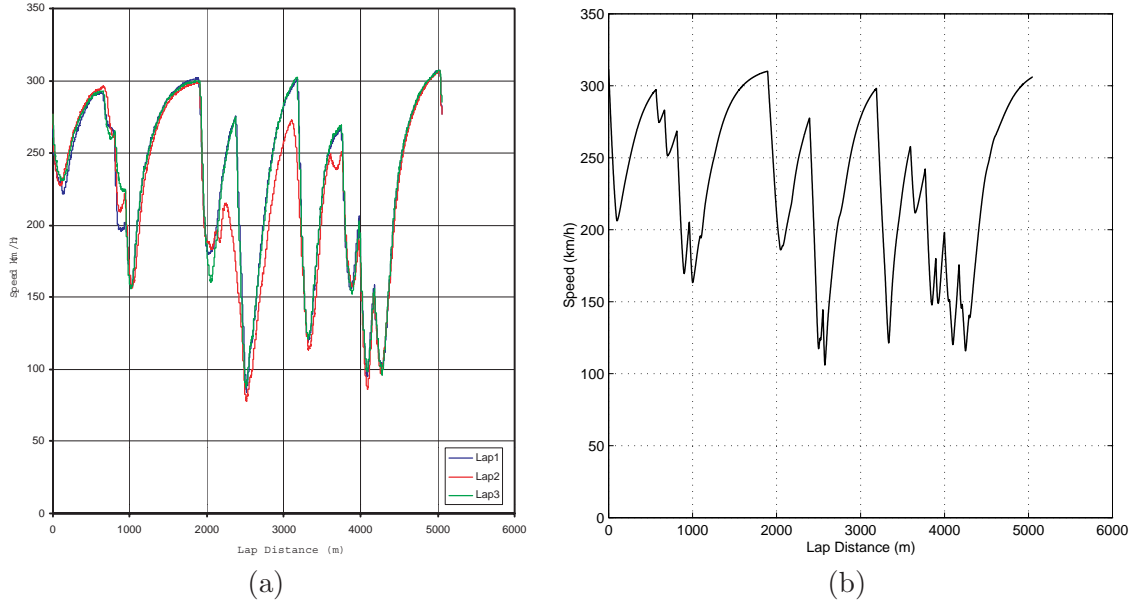

Figure 14: Velocity profiles through the Silverstone circuit: (a) achieved by human driver, (b) computed optimal.

3.2.13 Receding Horizon Implementation

When the environment is changing the optimal profile needs to be generated on-line. One way to achieve this is for the trajectory optimization to be implemented in a receding horizon scheme rather than executed in one shot, from the start point to the end point. In [12] numerical optimization along with a receding horizon scheme was used for trajectory planning of an autonomous vehicle maneuvering through obstacles. By including the distance between the end of the horizon and the final destination point in the total cost, it was shown that the vehicle reaches the final point. In [13] an extension of the previous optimization scheme was proposed in order to avoid the entrapment of the vehicle in concave obstacles. The main idea is that the cost function is estimated off-line for the whole area where the vehicle may move. Areas that may lead to entrapment are penalized and the estimated cost is taken into consideration in the total cost. Finally, in [14] the receding horizon strategy of [12] was combined with a "safety algorithm". The "safety algorithm" computes an "escape plan" from the end of the horizon to a "safe" state (such as the vehicle coming to a stop), for each optimization step. If such an "escape plan" is not feasible, then the last optimization step is not executed and the "escape plan" of the previous step is executed instead.

In this work we have assumed that the geometry of the trajectory is computed separately and it is provided to the velocity optimizer beforehand. Therefore, during a receding horizon implementation we assume that it is the job of the path planner to provide a feasible path that

ensures obstacle avoidance and guarantees that the vehicle will reach its final destination. This can be achieved by following the same strategy as in [12],[13] and [14]. However, guarantees that the velocity will not exceed the critical value at any point, and that there exists an "escape plan" at the end of each optimization step, will have to be provided before the velocity optimizer is implemented in a receding horizon scheme. Below we propose a dynamic scheme to adaptively choose the planning and execution horizons to provide such guaranties.

3.2.14   Receding Horizon Scheme

Figure 15 shows a schematic that demonstrates how the receding horizon scheme works. The *Planning Horizon* (PH_i) is the distance from the current position up to the point which the ith optimization step is performed. The *Execution Horizon* (EH_i) is a fraction of PH_i and it is the distance up to the point which the planned optimization will actually be executed. When the vehicle reaches the *Replanning Horizon* RH_i, which is a fraction of EH_i, the optimization is performed again up to the new planning horizon PH_{i+1}.
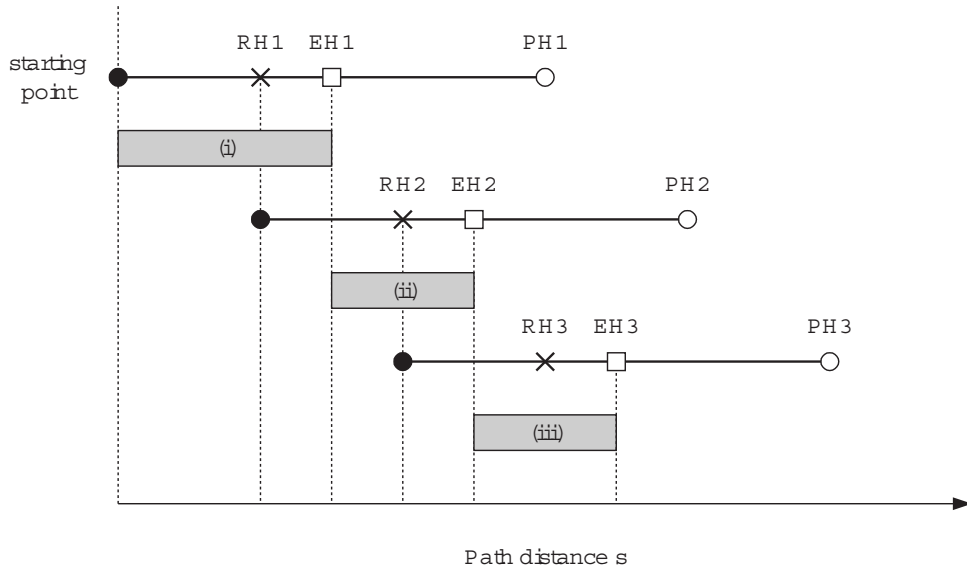

Figure 15: Optimization with receding horizon.

Let the vehicle be at the starting point ($s = s_0$ in Fig. 15). The optimization methodology is applied up to PH_1. After the optimization is completed, the vehicle may start executing the optimal trajectory up to EH_1. The shadowed area (i) in Fig. 15 shows the portion of the first optimization that is actually executed. When the vehicle reaches RH_1 the optimization is applied again from the current position RH_1 to the new planning horizon PH_2. The portion of the second optimization that will be actually executed is from EH_1 to EH_2 and it is shown as the shadowed area (ii) in Fig. 15. The process will end when the final destination is within the execution horizon. The distance between RH_i and EH_i is chosen such that enough time is allowed for the computation of the optimal trajectory from RH_i to PH_{i+1} before EH_i is reached. If the computation is instantaneous RH_i and EH_i can coincide. As already mentioned, the semi-analytical nature of the proposed algorithm results in minimal computational cost and thus from now on we will assume that the replanning and execution horizons coincide.

3.2.15 Robustness guarantees

In this section we propose an implementation scheme for the receding horizon optimization of the velocity profile along a given path. In particular, we propose a dynamic scheme to determine planning and execution horizons in the z_1 domain and guarantee the existence of an "escape plan" in the end of each executed subarc.

We propose the following formula to determine the planning horizon of the ith optimization step

$$\text{PH}_i = \max\{Tv_i, \text{PH}_{\min}\}, \tag{53}$$

where v_i is the vehicle velocity at the position of the execution horizon of the previous optimization step EH_{i-1}, $v_i = z_2(\text{EH}_{i-1})$, T is a constant "reaction" time, and $\text{PH}_{\min}$ is the minimum planning horizon (typically for $v_i = 0$). This is not unlike the way a human driver chooses a planning horizon, that is, the larger the velocity, the longer the "look ahead" distance needs to be. At the initial point A on the path, for the first optimization step $i = 1$ we have

$$\text{EH}_0 = z_1^A. \tag{54}$$

The optimal solution from the current position EH_{i-1} to PH_i is calculated using (52) and is denoted by $^i z_2^*(z_1)$.

Next, we construct the characteristic from $(z_1 = \text{PH}_i, z_2 = 0)$ integrating backwards in time using $u = -1$. This characteristic is denoted by $^i z_2^{\text{esc}}(z_1)$ and is referred to as *escape trajectory* of the ith optimization step. We choose the execution horizon for the ith optimization step as follows:

$$\text{EH}_i = \left\{ z_1 : \ ^i z_2^*(z_1) = \ ^i z_2^{\text{esc}}(z_1), \ z_1 \in [\text{EH}_{i-1}, \text{PH}_i] \right\}. \tag{55}$$

In the case when

$$\{(z_1, {}^i z_2^*(z_1)), z_1 \in [\text{EH}_{i-1}, \text{PH}_i]\} \bigcap \{(z_1, {}^i z_2^{\text{esc}}(z_1)), z_1 \in [\text{EH}_{i-1}, \text{PH}_i]\} = \varnothing \tag{56}$$

we need to increase T in (53) to determine a longer planning horizon until we can find the intersection point of the optimal solution and the escape trajectory (55).

At the end of each executed subarc EH_i we optimize up to the new planning horizon PH_{i+1}. The vehicle can decelerate enough to negotiate any corner outside PH_i since we have guaranteed that the vehicle starting from EH_i can come to a complete stop at PH_i. In case an obstacle exists after PH_i the vehicle can follow the escape trajectory to avoid collision. The Receding Horizon optimization scheme terminates when the end point B is within the execution horizon, namely $z_1^B \leq \text{EH}_i$ for some i.

The proposed implementation is summarized in the block diagram of Fig. 15. The first optimization step using the above Receding Horizon scheme on the general case path of Section 3.2.11 is shown in Fig. 17. Let the planning horizon PH_1 from (53) be at 30m as in Fig. 17. The execution horizon EH_1 is determined by the intersection of $^1 z_2^*$ and $^1 z_2^{\text{esc}}$. Observe that the solution generated by this implementation coincides with the infinite horizon solution of Section 3.2.11. If we randomly choose PH_x and EH_x as in Fig. 17 we run the risk of reaching unacceptably high velocities. For example, the critical velocity at P_1 does not allow the vehicle to decelerate enough and negotiate the sharp turn at P_2. In this case notice that there is no intersection point between the optimal solution and the escape trajectory (characteristic $^x z_2^{\text{esc}}$) and thus we need to increase T and choose a longer initial planning horizon.
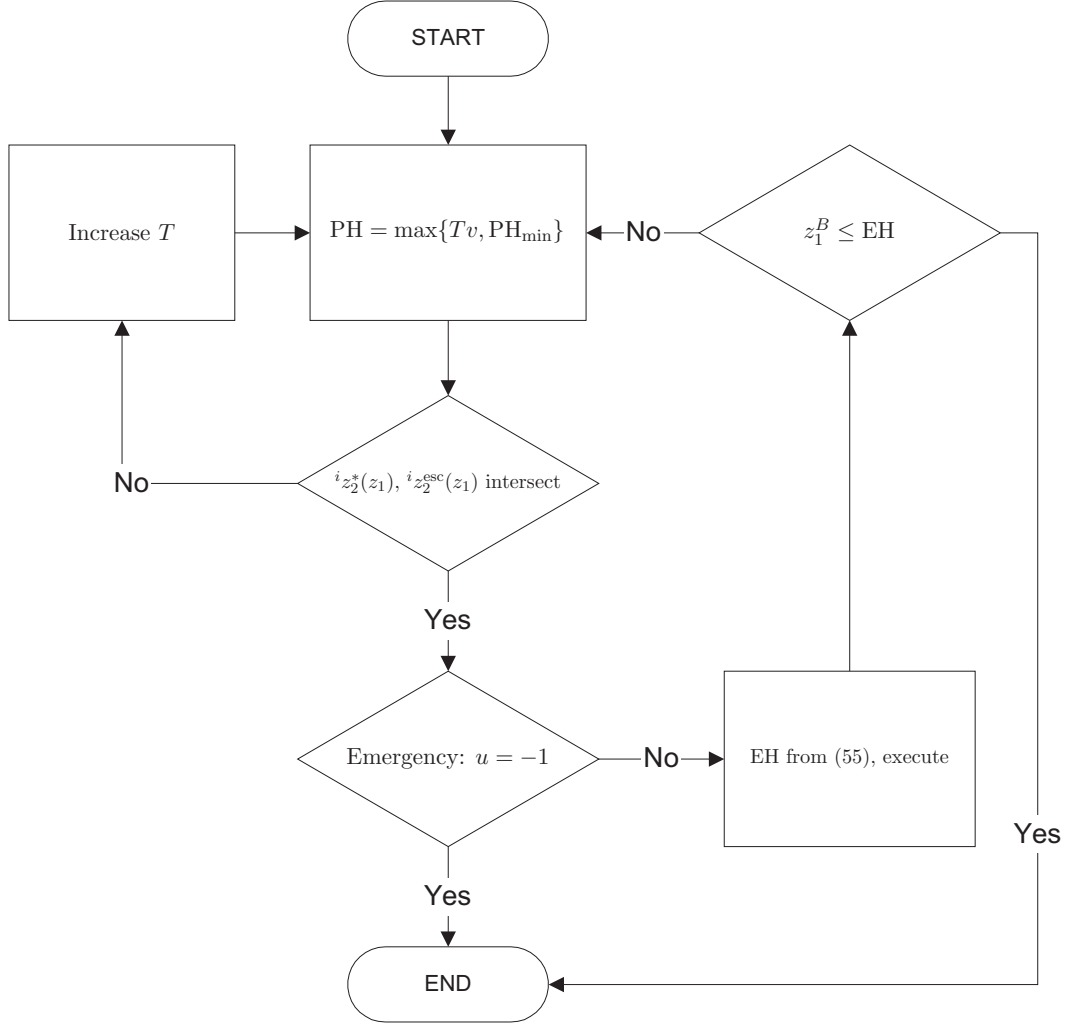
Figure 16: Receding Horizon implementation block diagram.

3.2.16 Numerical Example (Receding Horizon Implementation)

In this section we apply the proposed receding horizon algorithm to the F1 car trajectory of Section 3.2.12. We have chosen $T = 5$ sec, which for this example is enough for the "emergency stop" characteristic to intersect the optimal solution within the planning horizon for each iteration. The minimum planning horizon was chosen as $\text{PH}_{\min} = 200$ m.

In Fig. 18 the results of the first five steps of the receding horizon scheme are shown, along with the planning and execution horizons of each step. The solution (solid line) is compared with the infinite-horizon solution of the optimal velocity generator of Section 3.2.12 (dotted line). The two solutions coincide, thus confirming the validity of the proposed receding horizon scheme.
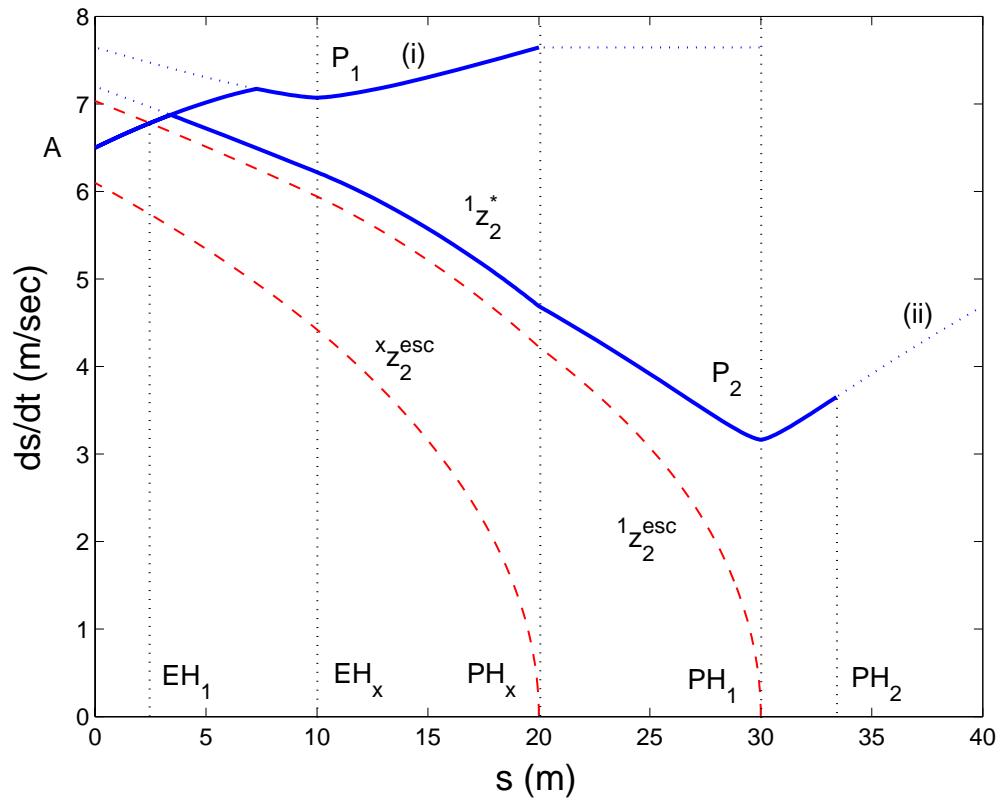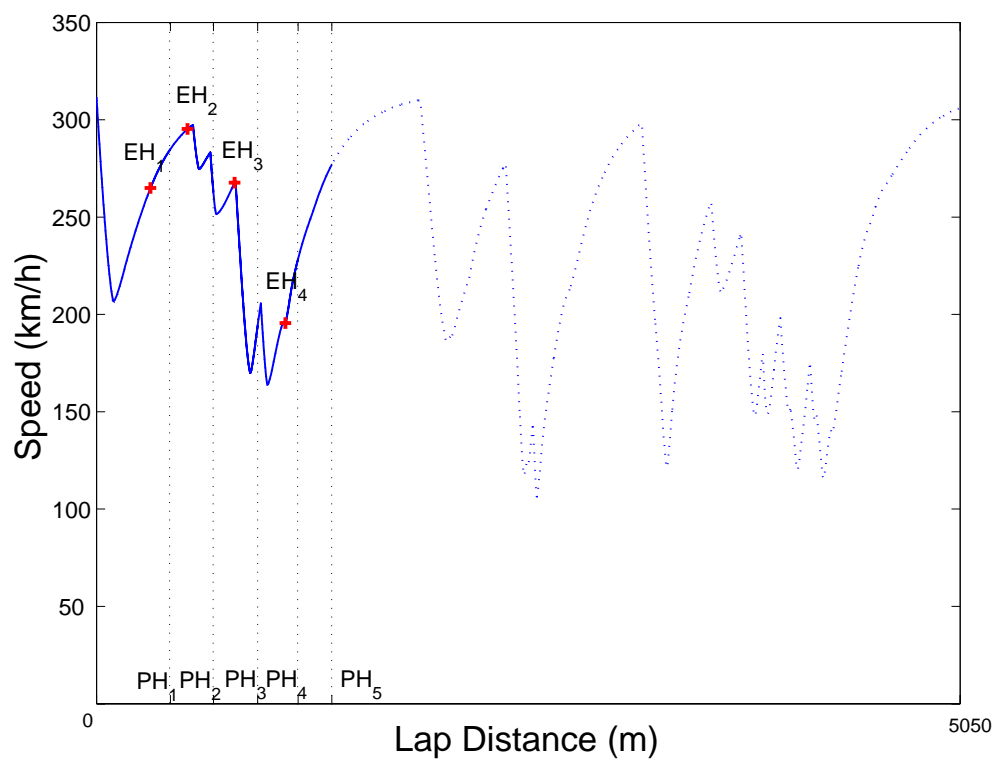
Figure 17: Dynamic scheme for determination of EH_i.

Figure 18: Optimization with receding horizon for the Silverstone circuit.

3.3 Extension to the Half-Car Model

Our next goal is to extend the algorithm presented above for optimal velocity profiles to a half-car model, which includes the yaw dynamics of the vehicle. The key ingredients for such an extension are the characterization of the acceleration envelope of the half-car model and the calculation of maximum acceleration and deceleration on a prescribed path.

3.3.1 The Half-Car Model

The equations of motion of a half-car model along a prescribed path $R(s)$ as in Fig. 19, are given below

$$m\ddot{x} = (f_{Fx} + f_{Rx})\cos\psi - (f_{Fy} + f_{Ry})\sin\psi, \tag{57}$$

$$m\ddot{y} = (f_{Fx} + f_{Rx})\sin\psi + (f_{Fy} + f_{Ry})\cos\psi, \tag{58}$$

$$I_z\ddot{\psi} = f_{Fy}\ell_F - f_{Ry}\ell_R. \tag{59}$$

In the above equations m is the vehicle's mass, I_z is the polar moment of inertia of the vehicle, and x and y are the cartesian coordinates of the center of mass (C.M.) in the inertial frame of reference; ψ is the yaw angle of the vehicle, and f_{ij} ($i = F, R$, $j = x, y$) denote the friction forces of the front and rear wheels, respectively, along the longitudinal and lateral body axes. Equations (2) will also be used, with $ds/dt = v = \sqrt{\dot{x}^2 + \dot{y}^2}$, and f_t, f_n the components of the resultant force, due to front and rear wheel friction, along the tangential and normal directions of travel respectively.

The path angle ϕ and the vehicle slip angle β (see Fig. 19) are given by

$$\phi = \arctan(\dot{y}/\dot{x}), \quad \beta = \phi - \psi, \tag{60}$$
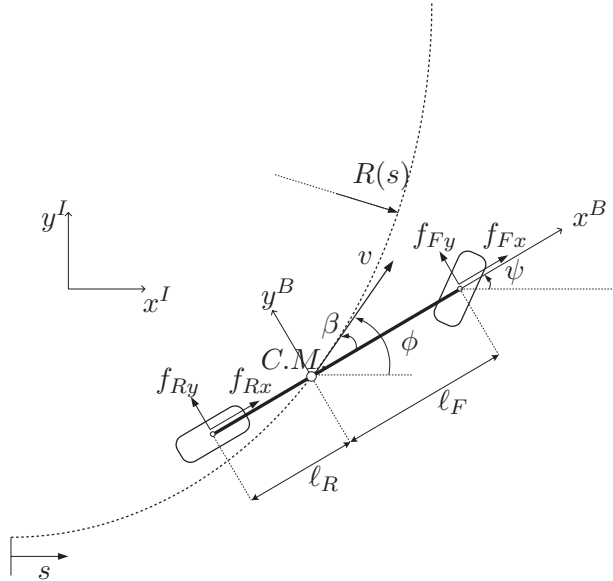
respectively.

Figure 19: A half-Car Model of a vehicle driving along a prescribed path $R(s)$.

31

3.3.2 Acceleration Envelope of the Half-Car Model

The equations of motion (57)-(59) are expressed in terms of the friction forces generated by the front and rear tires f_{ix} and f_{iy}, $i = F, R$. In the following calculation of the acceleration envelope of the half-car model we neglect power limitations from the engine/transmission. Such an assumption is more realistic when the vehicle is operating on surfaces of low friction coefficient, such as wet road or dirt, where the adhesion limits of the tires are considerably reduced and dominate in the calculation of the overall acceleration capacity of the vehicle.

The tire friction forces are calculated using Pacejka's "Magic Formula" model [18] as follows.

$$f_{ij}^{\text{tire}} = -\frac{s_{ij}}{s_i} F_i, \quad i = F, R \text{ and } j = x, y, \tag{61}$$

where, f_{ij}^{tire} ($i = F, R$ and $j = x, y$) are the components of the front and rear wheel friction forces along the longitudinal and lateral tire axes respectively, s_{ix} is the longitudinal and s_{iy} is the lateral slip of the i wheel. The components f_{ij}^{tire} should not be confused with the components f_{ij} of the same forces along the longitudinal and lateral body axes, used in equations (57)-(59). In particular,

$$f_{Rj} = f_{Rj}^{\text{tire}}, \quad j = x, y \tag{62}$$

$$f_{Fx} = f_{Fx}^{\text{tire}} \cos \delta - f_{Fy}^{\text{tire}} \sin \delta \tag{63}$$

$$f_{Fy} = f_{Fx}^{\text{tire}} \sin \delta + f_{Fy}^{\text{tire}} \cos \delta, \tag{64}$$

where δ is the steering angle of the front wheel.

The total friction force of the front and rear wheel, F_i ($i = F, R$), is computed using

$$F_i = F_{iz} D \sin(C \operatorname{atan}(B s_i)), \quad i = F, R, \tag{65}$$

where F_{iz} ($i = F, R$) is the vertical load at the front and rear axle, respectively, and the total slip s_i ($i = F, R$) is computed as

$$s_i \triangleq \sqrt{s_{ix}^2 + s_{iy}^2} \text{ with } i = F, R. \tag{66}$$

The friction force of each wheel lies within a circle of radius equal to the maximum friction force $f_i^{\max}$ ($i = F, R$), attained at $s_i^{\max}$, from (65). This is shown in Fig. 20.

We assume in the sequel that we can control the longitudinal slip s_{ix}, of the front and rear wheel independently, as well as the steering angle δ of the front wheel. Independent longitudinal slip of front and rear wheels is a realistic assumption for modern vehicles equipped with variable ratio torque distribution systems such as Acura's SH-AWD and BMW's XDrive. Similarly, independent longitudinal front and rear wheel slip control can be achieved by expert rally drivers via advanced driving techniques, such as "left foot braking" and "handbrake cornering" [4]. Using the standard definition of longitudinal slip [18] we choose $s_{ix} \in [-1, +1]$.

The expressions for the lateral slip of the front and rear wheels can be computed from

$$s_{Ry} \triangleq \frac{v \sin \beta - \dot\psi \ell_R}{v \cos \beta}, \tag{67}$$

$$s_{Fy} \triangleq \frac{v \sin(\beta - \delta) + \dot\psi \ell_F \cos \delta}{v \cos(\beta - \delta) + \dot\psi \ell_F \sin \delta}. \tag{68}$$

The rear lateral slip s_{Ry} is determined solely by the states of the system, i.e., s_{Ry} is fixed for a given operating condition of the vehicle (v, β, $\dot\psi$). Thus, for a given operating condition of the
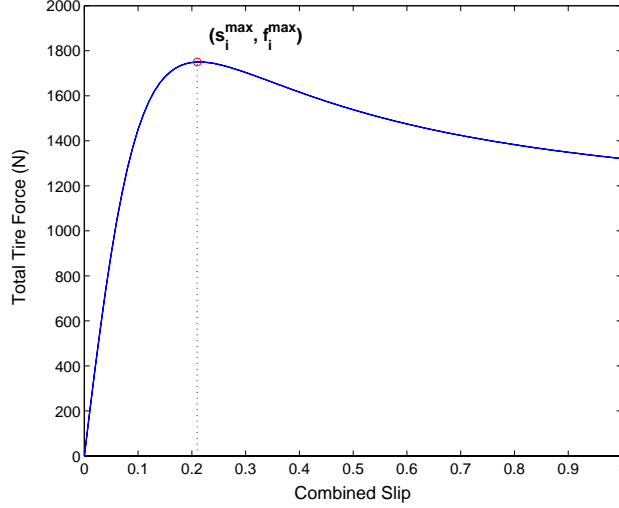
Figure 20: Total friction force of the ith wheel with respect to the combined slip as given by the Magic Formula.

vehicle, and assuming that we can control the rear longitudinal slip, the rear friction force f_R lies on a characteristic curve $\mathcal{F}_R(s_{Ry})$ as in Fig. 21. That is,

$$f_R = (f_{Rx}, f_{Ry}) \in \mathcal{F}_R(s_{Ry}). \tag{69}$$

The front lateral slip s_{Fy}, however, depends on the steering angle δ, which is one of the control variables. In Fig. 22 we demonstrate that for any vehicle operating condition we may generate any front wheel lateral slip, $s_{Fy} \in [-s_F^{\max}, +s_F^{\max}]$ using a steering angle δ within a realistic range of $\delta \in [-\pi/4, +\pi/4]$. In Fig. 21 it is also demonstrated that the whole friction circle including its interior can be constructed by characteristics of s_{Fy} in the interval $[-s_F^{\max}, +s_F^{\max}]$. Thus, given any operating condition of the vehicle, and assuming that we can control independently the front longitudinal slip and steering angle, the front friction force f_F may be chosen anywhere inside the front wheel friction circle $\mathcal{F}_F$

$$f_F = (f_{Fx}, f_{Fy}) \in \mathcal{F}_F = \{f_F : |f_F| \le f_F^{\max}\}. \tag{70}$$

In Fig. 21 we demonstrate the case of a neutrally balanced vehicle (the C.M. in the middle of the wheelbase) with same tires in front and rear wheels. In a neutrally balanced vehicle $F_{Fz} = F_{Rz}$ in (65) and $f_F^{\max} = f_R^{\max}$ assuming same tires in front and rear wheels. Thus, for such a vehicle configuration, we conclude

$$\mathcal{F}_R(s_{Ry}) \subset \mathcal{F}_F \quad \text{and} \quad \mathcal{F}_F = \bigcup_{sRy} \mathcal{F}_R(s_{Ry}), \quad s_{Ry} \in [-s_R^{\max}, s_R^{\max}]. \tag{71}$$

At this point we assign f_R and f_F from (69) and (70) respectively to be the control variables of our system.

The resultant force envelope $\mathcal{F}_{GG}(s_{Ry})$ at the C.M. of the vehicle, referred to as GG-diagram in the vehicle dynamics literature [19], is constructed for each operating condition of the vehicle v, β, $\dot{\psi}$ (or equivalently s_{Ry}), by adding all available front and rear tire friction forces, as in Fig. 23. This operation is nothing more than the Minkowski sum [20] of the the front friction circle $\mathcal{F}_F$ and the rear wheel friction characteristic curve $\mathcal{F}_R(s_{Ry})$, namely,

$$\mathcal{F}_{GG}(s_{Ry}) = \mathcal{F}_F \oplus \mathcal{F}_R(s_{Ry}) \triangleq \{f_{GG} = f_F + f_R, \ f_F \in \mathcal{F}_F, \ f_R \in \mathcal{F}_R(s_{Ry})\}, \tag{72}$$
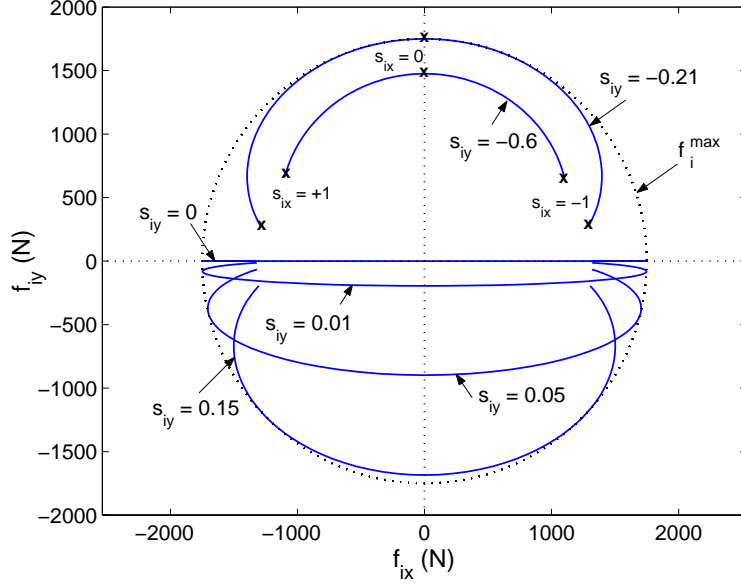
33

Figure 21: Front and rear tire friction characteristic curves for fixed lateral slip s_{iy} $(i = F, R)$ and longitudinal slip $s_{ix} \in [-1, +1]$ $(i = F, R)$.

where $f_{GG} = (f_{GGx}, f_{GGy})$ is the resultant force at the C.M. and its components along the longitudinal and lateral vehicle body axes, f_{GGx} and f_{GGy} respectively.

The optimal control strategy of Section 3.2.10 dictates that for minimum time travel the vehicle should use the maximum available acceleration or deceleration. This corresponds to $u = \pm 1$ in the case of the point mass model of Section 3.2.10. The maximum available acceleration for the half car model is given by the boundary of $\mathcal{F}_{GG}(s_{Ry})$ denoted by $\partial \mathcal{F}_{GG}(s_{Ry})$. Notice that for any $f_{GG}^*(s_{Ry}) \in \partial \mathcal{F}_{GG}(s_{Ry})$ there exists a unique vector $[f_F^*(s_{Ry}), f_R^*(s_{Ry})]$, where $f_F^*(s_{Ry}) \in \mathcal{F}_F$ and $f_R^*(s_{Ry}) \in \mathcal{F}_R(s_{Ry})$, such that $f_{GG}^*(s_{Ry}) = f_F^*(s_{Ry}) + f_R^*(s_{Ry})$. In other words, one can define the following one-to-one mapping

$$\mathcal{M} : \mathcal{F}_F \times \mathcal{F}_R(s_{Ry}) \mapsto \partial \mathcal{F}_{GG}(s_{Ry})$$
$$f_{GG}^*(s_{Ry}) = \mathcal{M}(f_F^*(s_{Ry}), f_R^*(s_{Ry})) \tag{73}$$

and its inverse

$$(f_F^*(s_{Ry}), f_R^*(s_{Ry})) = \mathcal{M}^{-1}(f_{GG}^*(s_{Ry})). \tag{74}$$

An extension of the optimal control strategy described in Section 3.2.10 becomes now evident. Given an operating condition of the vehicle (velocity components $\dot{x}$ and $\dot{y}$, orientation ψ and yaw rate $\dot{\psi}$) and the geometry of the path $\kappa(s)$, we can calculate the necessary centripetal force f_n from (2) such that the vehicle follows the path. We can also determine the tangential and normal directions to the path with respect to the orientation of the vehicle (these are denoted by e_t and e_n respectively in Fig. 23). The calculated f_n lies along the normal direction e_n and may be produced by only two possible total forces f_{GG}^{*+} and f_{GG}^{*-} on $\partial \mathcal{F}_{GG}$ (Fig. 23). The force f_{GG}^{*+} produces an accelerating tangential force f_t, which corresponds to the $u = +1$ strategy of Section 3.2.10, and f_{GG}^{*-} produces a braking force that corresponds to the $u = -1$ strategy. Using the map $\mathcal{M}^{-1}$ of (74) with either f_{GG}^{*+} or f_{GG}^{*-} we can determine the required friction forces at the front and rear wheels $f_F = (f_{Fx}, f_{Fy}) = f_F^*$, $f_R = (f_{Rx}, f_{Ry}) = f_R^*$ respectively (Fig. 24). We can use these expressions to integrate equations (57)-(59).
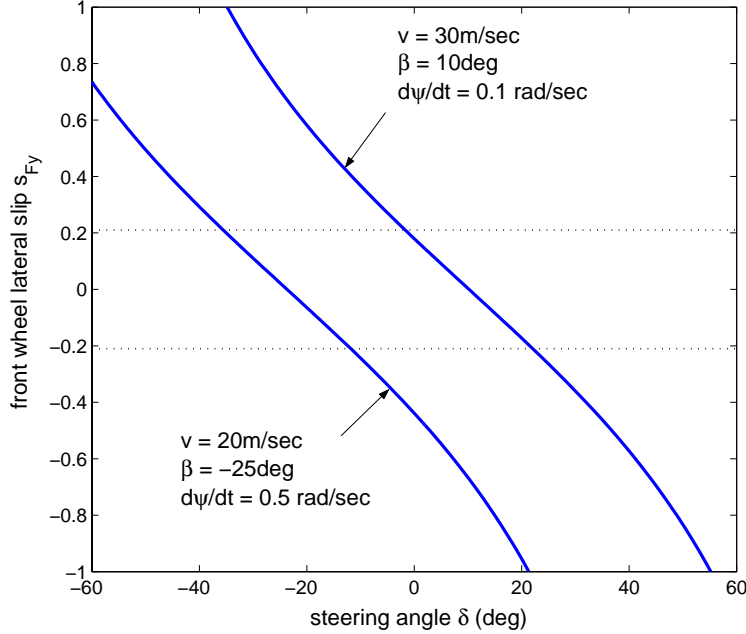
34

Figure 22: Front lateral slip with respect to steering angle for given operating condition of the vehicle.

3.3.3 Direct Implementation of the Point Mass Strategy

In the previous section we calculated the acceleration capacity of a half-car model and derived the maximum available acceleration/deceleration when the vehicle tracks a prescribed path. Next, we demonstrate a direct implementation of the optimal control strategy of Section 3.2.10 to a path with a point of minimum magnitude of radius using the equations of motion (57)-(59) and acceleration capacity (72) of the half-car model. The solution along sub-arcs of the overall path containing a single point of minimum radius is the main "building block" in the construction of the optimal solution along the total path using the methodology of Section 3.2.10. The second "building block" is the solution along paths of constant radius. An extension of the optimal control strategy along a constant radius path to a half-car model is straightforward (steady-state cornering of constant velocity [19, 21] using maximum centripetal acceleration) and will be omitted.

Consider the path of Fig. 25(a) with radius profile as shown in Fig. 25(b). Notice that at point $P_1(x_{P_1}, y_{P_1})$ of the path the radius profile takes its minimum value $R(s) = R_{P_1}$ at $s = s_{P_1}$. According to the methodology of Section 3.2.10 the velocity of the vehicle is equal to v_{crit} at s_{P_1} such that the generated centripetal force matches the total acceleration capacity of the vehicle. The vehicle decelerates with maximum available deceleration ($u = -1$) before the point P_1 and accelerates with maximum available acceleration ($u = +1$) after the point P_1.

Our first task is to determine the critical velocity $v_{\text{crit}}(s_{P_1})$ of the half-car model at P_1 such that the total acceleration capacity is used towards the generation of the centripetal force. As demonstrated in Section 3.3.2 the acceleration capacity of the half-car model depends on its state of operation v, β and $\dot{\psi}$. We conclude that $v_{\text{crit}}(s_{P_1})$ is different for all possible values of β and $\dot{\psi}$ at s_{P_1}. For consistency we enforce the following attitude and attitude rate restrictions

$$\beta(s_{P_1}) = 0, \quad \dot{\psi}(s_{P_1}) = v(s_{P_1})/R_{P_1}. \tag{75}$$

The conditions (75) above imply that the vehicle satisfies the steady-state cornering requirements
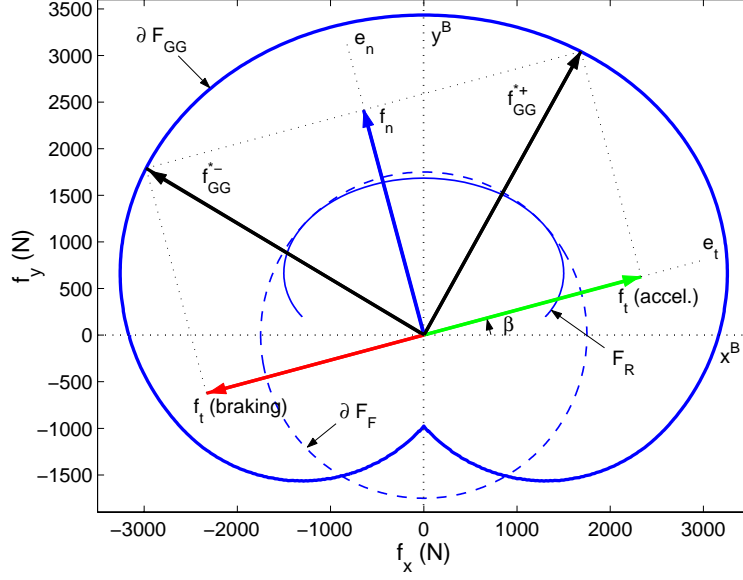
35

Figure 23: GG-diagram for a given operating condition of the vehicle.

[19, 21], instantaneously at the point of minimum radius P_1.

Conditions (75) imply that the lateral slip of the rear wheel at P_1, from (67), is

$$s_{Ry}(s_{P_1}) = -\ell_R/R_{P_1}. \tag{76}$$

The rear tire force along the normal direction n coincides with f_{Ry} at s_{P_1}, and is maximized when $f_{Rx}(s_{P_1}) = 0$. Recall that we may use any front tire force within the friction circle of radius $f_F^{\max}$. In order to maximize the contribution of the front tire to the centripetal force we choose $|f_{Fy}(s_{P_1})| = f_F^{\max}$ and $f_{Fx}(s_{P_1}) = 0$.

Thus, the velocity of the half-car model at point P_1 is given by

$$v_{\mathrm{crit}}(s_{P_1}) = \sqrt{\frac{|R_{P_1}|(f_F^{\max} + |f_{Ry}(s_{P_1})|)}{m}}. \tag{77}$$

The trajectory of the vehicle in Fig. 26 is constructed according to the optimal control strategy of Section 3.2.10.

The acceleration phase is constructed by integration forward in time of the equations of motion (57) - (59) starting from point P_1 with initial conditions (75), (77) using f_{GG}^{*+} from Section 3.3.2.

The braking phase is constructed by integration backwards in time of the equations of motion (57) - (59) starting from point P_1 with initial conditions (75), (77) using f_{GG}^{*-} from Section 3.3.2.

The resulting velocity profile is shown in Fig. 27(a) and the vehicle slip angle β is shown in Fig. 27(b). The longitudinal, lateral and total friction forces, f_{ix}, f_{iy} and f_i, $i = F, R$, of the front and rear tires are shown in figures 28(a) and 28(b) respectively.

In both accelerating and braking phases, we notice an increase in the magnitude of the vehicle slip angle β and in particular, an oversteering tendency of the vehicle. Oversteer occurs when the rear wheels reach the adhesion limit and cannot generate any additional cornering force, while the tires of the front axle either operate away from the adhesion limit [19]. In case both front and rear tires have reached their adhesion limit, oversteer occurs when the yawing moment due to the front tire friction is greater than the one due to the rear tire friction. Oversteer appears as a

Figure 24: Using $\mathcal{M}^{-1}$ we can calculate the front and rear axle forces f_F and f_R when the vehicle operates at the limit of its acceleration capacity: Maximum deceleration case f_{GG}^{*-}.

"nose-in" spin of the vehicle (Fig. 26), i.e. when the vehicle slip angle develops in a direction such as $\beta\,\mathrm{sign}(R) < 0$.

For the numerical example of Section 3.3.3 we consider equal distribution of the weight in front and rear axles ($\ell_F = \ell_R$) and same tires in front and rear axles. For such a vehicle configuration (71) holds and we conclude that

$$\max(|f_{Ry}(s_{Ry})|) \leq \max(|f_{Fy}(s_{Ry})|), \tag{78}$$

for any vehicle operating condition $v, \beta, \dot{\psi}$. The later explains the oversteering tendency of the vehicle in Fig. 26.

In Section 3.2.10 the optimal trajectory along the total path is constructed by concatenation of the optimal trajectories along specific sub-arcs, namely, sub-arcs containing a point of minimum radius and sub-arcs of constant radius. Continuity of the states in the point mass model case of Section 3.2.10 is achieved by switching between trajectories at the intersection points of the $z_2(z_1)$ profiles of each sub-arc.

In the half-car model case the state vector is extended to include the yaw dynamics of the vehicle (β, $\dot{\psi}$). In constructing a trajectory over the total path by concatenation of trajectories over sub-arcs of the total path, we have to ensure continuity of all states (v, β, $\dot{\psi}$) at the switching points from one sub-arc trajectory to the other. A necessary condition for the continuity of the yaw states at the switching points between trajectories is that the yaw states remain bounded. In the following we present a stable implementation of the methodology of Section 3.2.10 with respect to the yaw dynamics.
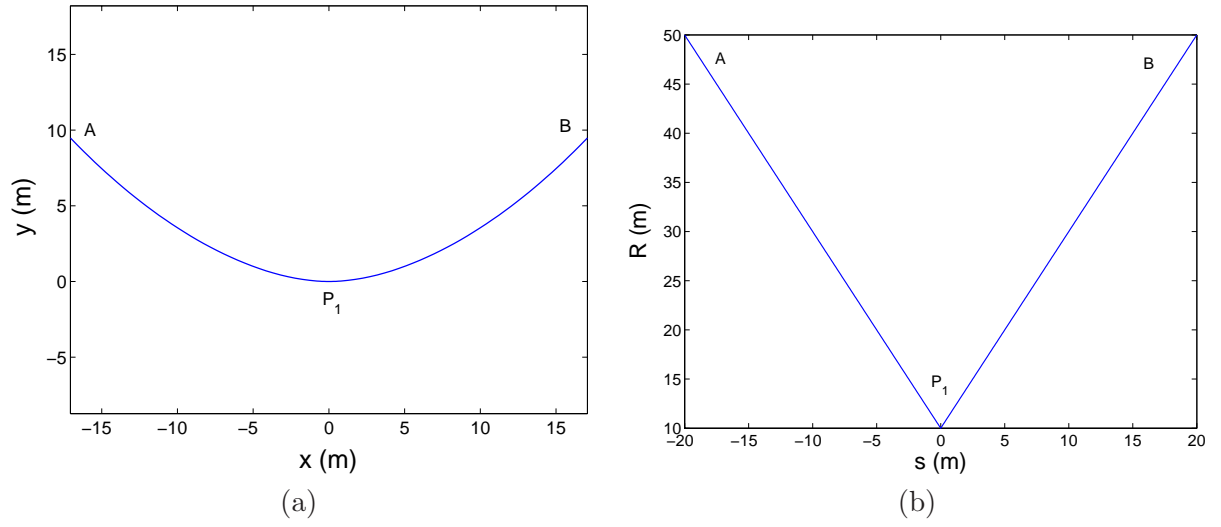
Figure 25: (a) A corner with a point of minimum radius. (b) Radius profile of the corner.
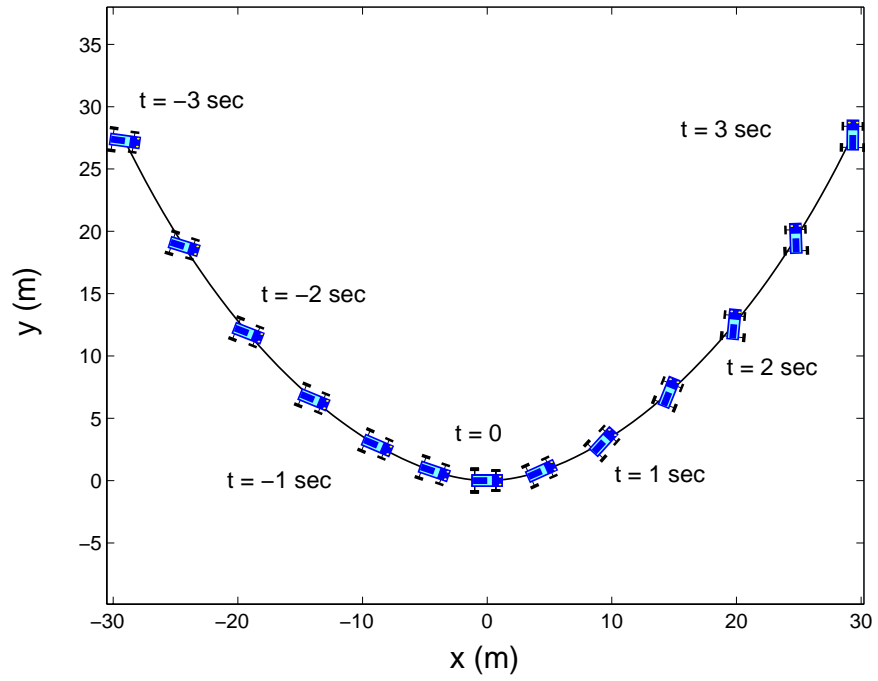

Figure 26: Direct implementation of the optimal control strategy to the half-car model: trajectory.
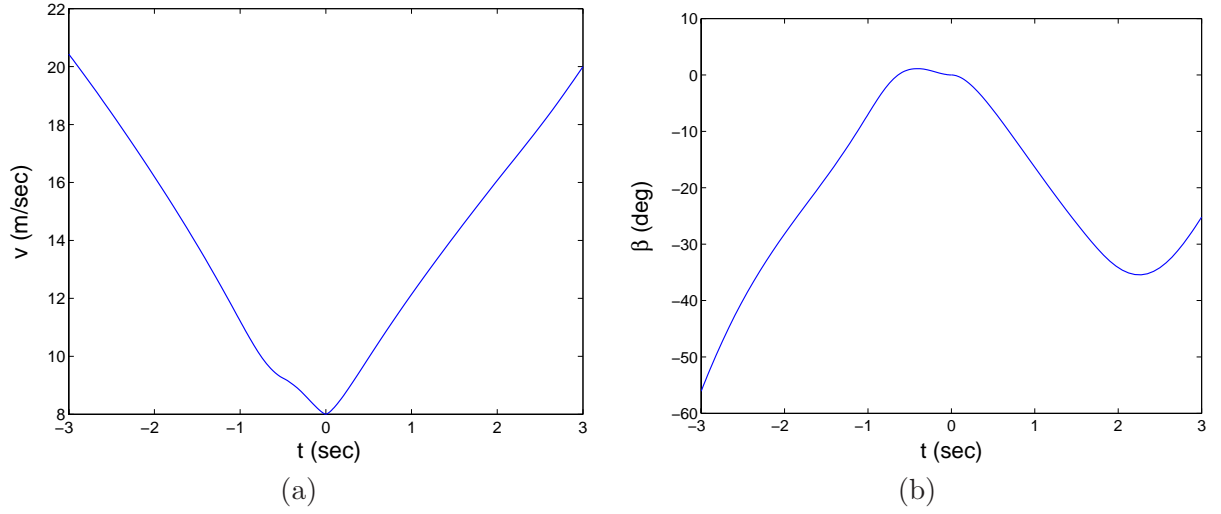
Figure 27: Direct implementation of the optimal control strategy to the half-car model: (a) velocity profile (b) vehicle slip angle.
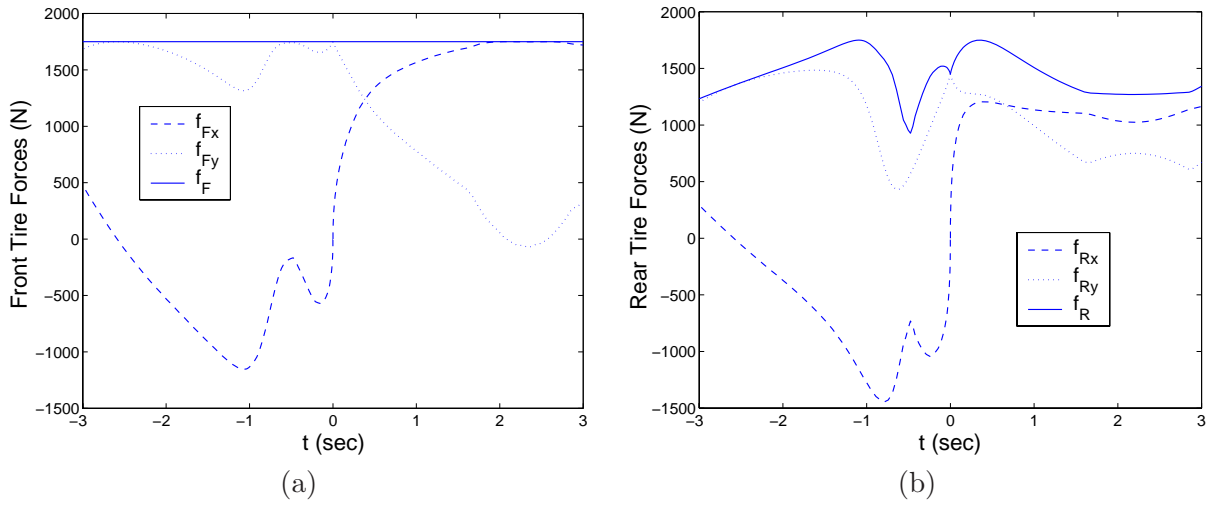

Figure 28: Direct implementation of the optimal control strategy to the half-car model: front and rear tire forces.

3.3.4 Stable Implementation of the Point Mass Methodology

Vehicle yaw stability characteristics vary with the different possible configurations of the vehicle: weight distribution, front-rear-all wheel drive, etc [19]. In this work we demonstrate the importance of yaw stability in relation to the problem of generating near-minimum-time velocity profiles along prescribed paths, rather than address the problem of vehicle stability for all possible configurations. For demonstration purposes we will consider the neutrally balanced vehicle of Section 3.3.3 with same tire characteristics and an inherent oversteering behavior as described therein.

In this section we design a control scheme in which the optimal $f_{GG}^{*\pm}$ strategy is interrupted momentarily by a control law aiming to reduce the magnitude of the vehicle slip angle. We define the objective of the stabilizing control law as follows: (i) guarantee that the vehicle remains on the prescribed path, and (ii) generate yaw moment to oppose oversteer.

3.3.5 Stabilizing Control

Consider the following control strategy. Let both forces on the front and rear axles be parallel to the normal direction to the path, i.e.

$$\langle f_i, e_t \rangle = 0, \quad i = F, R \tag{79}$$

where $\langle ., . \rangle$ denotes the vector inner product and e_t is the unit vector along the tangential to the path direction.

In order for the vehicle to remain on the prescribed path $R(s)$ we require that the total force, which lies on the normal direction to be equal to the centripetal force

$$f_F + f_R = f_n = \frac{mv^2}{R(s)} \tag{80}$$

where v is the current speed of the vehicle. It is obvious that the forces generated by the front and rear tires contribute only to the centripetal acceleration of the vehicle and thus the speed remains constant.

$$\dot{v} = 0. \tag{81}$$

The operation of the control strategy (79), (80) is demonstrated in Fig. 29. For a given operating condition of the vehicle $(v, \beta, \dot{\psi})$ the rear tire force $f_{Ry}(s_{Ry})$ lies on the characteristic curve $\mathcal{F}_R(s_{Ry})$. Given the condition (79) the rear tire friction force is determined uniquely as in Fig. 29. In the same figure we notice that the front tire force is also uniquely determined in order for the condition (80) to be satisfied.

Next, we derive the switching function that determines the instances when the (79), (80) control must be activated. Recall equation (60) which associates the vehicle slip angle β, the vehicle yaw angle ψ and the path angle ϕ. Differentiating (60) twice we get

$$\dot{\beta} = \dot{\phi} - \dot{\psi} = \phi' v - \dot{\psi} = \frac{v}{R} - \dot{\psi} \tag{82}$$

$$\ddot{\beta} = -\frac{R'}{R^2}v^2 + \frac{1}{R}\dot{v} - \frac{1}{I_z}M_z \tag{83}$$

where M_z is the yaw moment given by

$$I_z\ddot{\psi} = M_z = \ell_F f_{Fy} - \ell_R f_{Ry} \tag{84}$$
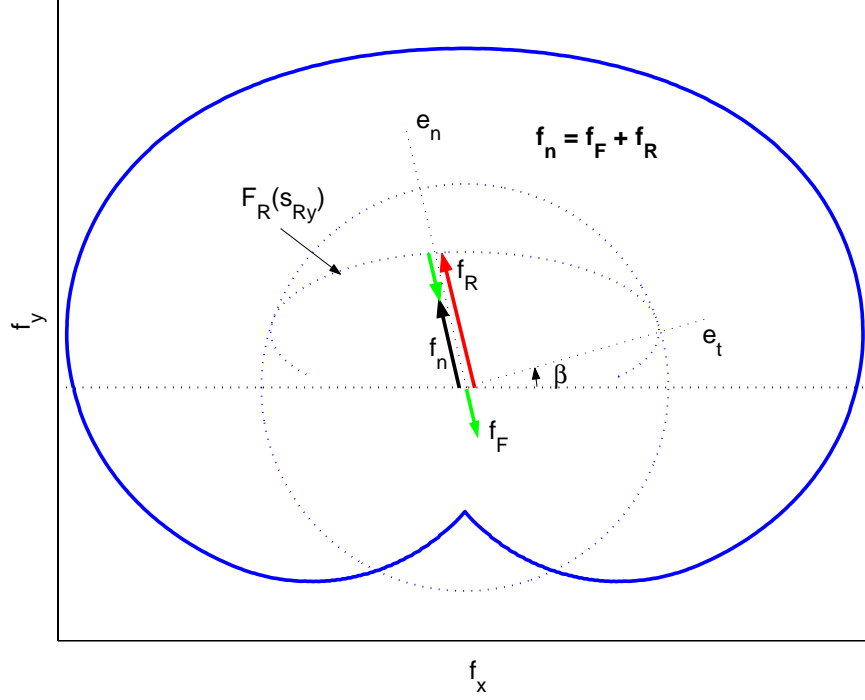
Figure 29: The front and rear wheel friction forces are uniquely determined in the yaw stabilization mode.

Consider the case where the control strategy (79), (80) is applied and condition (81) holds. Also let the control (79), (80) be activated when

$$s_{Ry} = s_R^{\max}. \tag{85}$$

Equation (85) is a necessary condition for oversteer, as it implies that the rear wheel has reached its adhesion limit. At this point we will have

$$f_{Ry} = \text{sign}(R) f_R^{\max} \tag{86}$$

$$f_{Fy} = \frac{mv^2}{R} - \text{sign}(R) f_R^{\max}, \tag{87}$$

and equation (83) can be written

$$\text{sign}(R)\ddot{\beta} = -\frac{\text{sign}(R)R'}{R^2}v^2 - \frac{1}{I_z}\left(\frac{\ell_F mv^2}{|R|} - (\ell_F + \ell_R)f_R^{\max}\right). \tag{88}$$

The yaw acceleration is opposing oversteer when

$$\text{sign}(R)\ddot{\beta} > 0. \tag{89}$$

Substituting (88) in (89) we get

$$v < \sqrt{\frac{R^2(\ell_F + \ell_R)f_R^{\max}}{I_z\text{sign}(R)R' + \ell_f|R|m}} \triangleq v_s \tag{90}$$

In summary, we have that switching from $f_{GG}^{*\pm}$ to (79), (80) when

$$s_{Ry} \le s_R^{\max} \quad \text{or} \quad v \ge v_s \tag{91}$$

results in a yawing acceleration that reduces oversteer.

41

3.3.6 Numerical Example 1: Single Corner

Consider the reference path of Fig. 25. The trajectory of the vehicle in Fig. 30 is constructed as follows:

The acceleration phase is constructed by integration forward in time of the equations of motion (57) - (59) starting from point P_1 with initial conditions (75), (77). The control switches from f_{GG}^{*+} to (79), (80) whenever the condition (91) holds.

The deceleration phase is constructed by integration backwards in time of the equations of motion (57) - (59) starting from point P_1 with initial conditions (75), (77). The control switches from f_{GG}^{*-} to (79), (80) whenever the condition (91) holds.

The resulting velocity profile is shown in Fig. 31(a) and the vehicle slip angle β is shown in Fig. 31(b). The longitudinal, lateral and total friction forces, f_{ix}, f_{iy} and f_i, $i = F, R$, of the front and rear tires are shown in figures 32(a) and (b) respectively.

We notice that we achieve a velocity profile comparable to the one using the direct implementation of Section 3.3.3. At the same time the vehicle slip angle remains bounded and oversteer is considerably reduced. Observing the intervals where the velocity remains constant (Fig. 31(a)) we can identify the switchings from $f_{GG}^{*\pm}$ to the stabilizing control strategy.
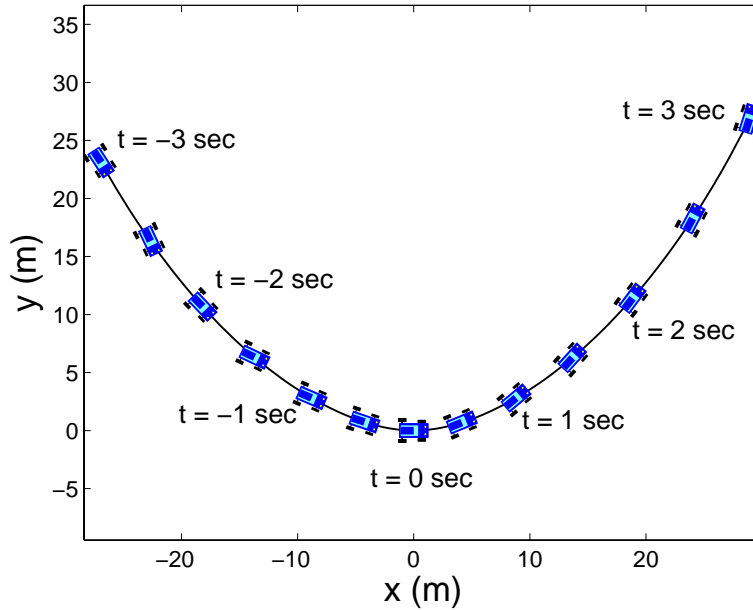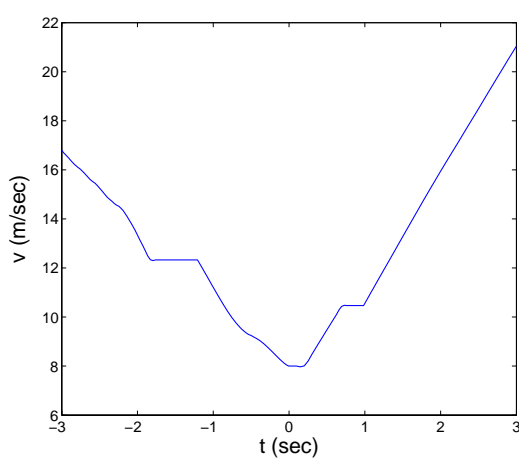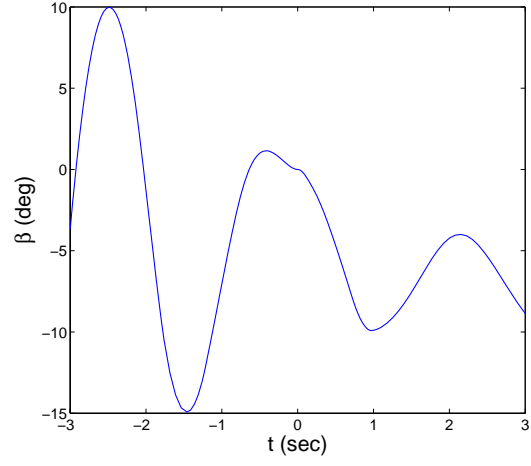

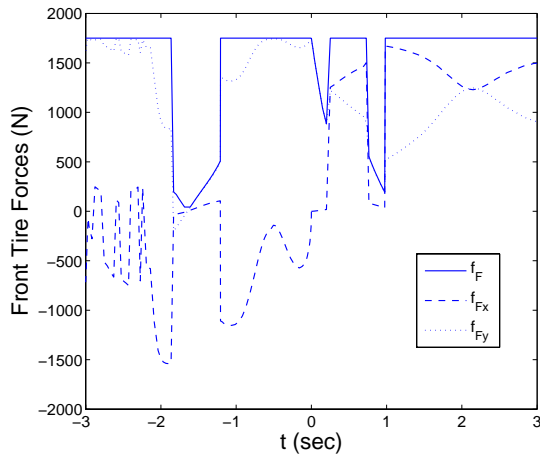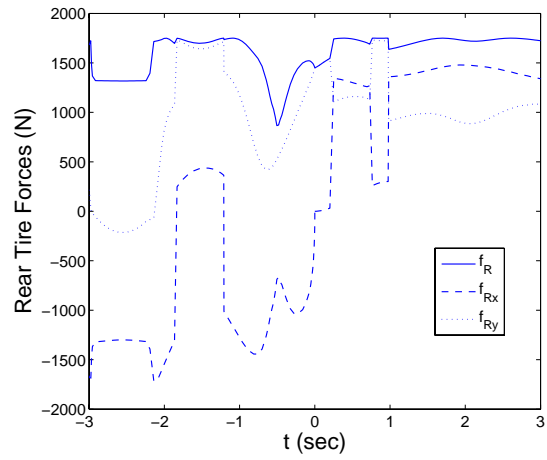Figure 30: Stable implementation of the optimal control strategy to the half-car model: trajectory.

Figure 31: Stable implementation of the optimal control strategy to the half-car model: (a) velocity profile (b) vehicle slip angle.

Figure 32: Stable implementation of the optimal control strategy to the half-car model: front and rear tire forces.

3.3.7 Numerical Example 2: Consecutive Corners

In this section we construct the trajectory along a path consisting of consecutive corners according to the methodology of Section 3.2.10, using the stable implementation of Section 3.3.4.

Consider the path of Fig. 33(a). In Fig. 33(b) we can see the corresponding curvature profile. Consider fixed initial and final velocities $v_0 = v_f = 10$m/sec at points A and B of the path respectively.
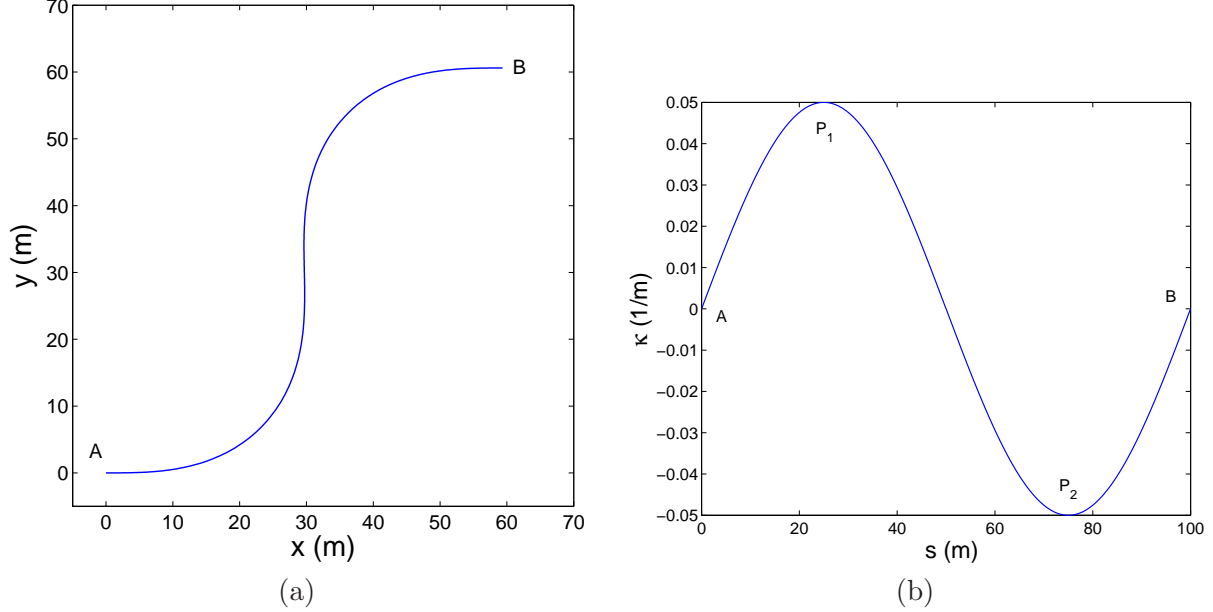

(a) (b)

Figure 33: (a) A path with two consecutive corners (b) Curvature profile of the path.

According to the methodology of Section 3.2.10 we construct the following trajectories:

Starting from point A with initial yaw states satisfying (75) and velocity v_0 we integrate forward in time the equations of motion (57) - (59). The control switches from f_{GG}^{*+} to (79), (80) whenever the condition (91) holds (stable implementation). The resulting velocity profile $V_A^+(s)$ is shown in Fig. 34 and the vehicle slip angle $\beta_A^+(s)$ in Fig. 35.

Starting from point B with initial yaw states satisfying (75) and velocity v_f we integrate backwards in time the equations of motion (57) - (59). The control switches from f_{GG}^{*-} to (79), (80) whenever the condition (91) holds (stable implementation). The resulting velocity profile $V_B^-(s)$ is shown in Fig. 34 and the vehicle slip angle $\beta_B^-(s)$ in Fig. 35.

Starting from point P_1 with initial conditions (75), (77) we integrate forward in time the equations of motion (57) - (59). The control switches from f_{GG}^{*+} to (79), (80) whenever the condition (91) holds. The corresponding velocity profile is $V_{P_1}^+(s)$ and the vehicle slip angle is $\beta_{P_1}^+$ in figures 34 and 35 respectively.

Starting from point P_1 with initial conditions (75), (77) we integrate backwards in time the equations of motion (57) - (59). The control switches from f_{GG}^{*-} to (79), (80) whenever the condition (91) holds. The corresponding velocity profile is $V_{P_1}^-(s)$ and the vehicle slip angle is $\beta_{P_1}^-$ in figures 34 and 35 respectively.

Finally we construct the velocity and vehicle slip angle profiles for P_2 $V_{P_2}^\pm$ and $\beta_{P_2}^\pm$ in figures 34 and 35 respectively, similar to the characteristics corresponding to point P_1.

In the point mass case (Section 3.2.10) the switching from one trajectory to the other is determined by the intersection points of the corresponding velocity profiles. In the half-car model,
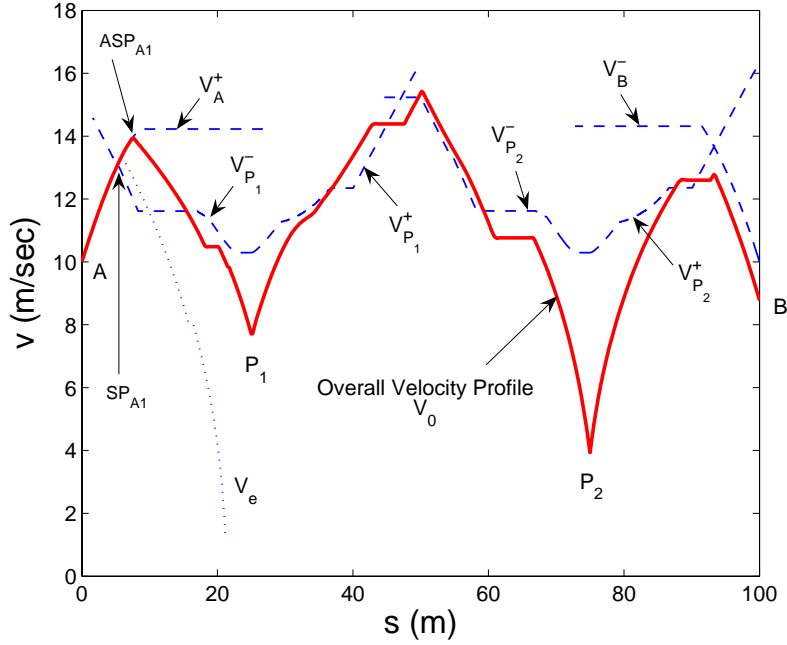
44

Figure 34: Stable implementation to consecutive corners: velocity profile.

where the state vector is extended by the yaw dynamics states, however the intersection points of the velocity profiles do not necessarily coincide with the intersection points of the vehicle slip angle. For instance $V_A^+(s)$ and $V_{P_1}^-(s)$ in Fig. 34 intersect at $s = 5.95$m (point SP_{A1}), while $\beta_A^+(s)$ and $\beta_{P_1}^-(s)$ intersect at $s = 6.3$m.

On the other hand, using the stable implementation of Section 3.3.4 to construct the trajectories along each sub-arc results in trajectories with bounded values of the yaw states. In other words the vehicle slip angle profiles are considerably close in the area of intersection of the corresponding velocity profiles. The switching points for the overall trajectory are chosen by trial and error, in the area of intersection of the velocity profiles aiming to generate a velocity profile

$$V_o(s) \simeq \min_s \{V_A^+(s), V_{P_1}^-(s), V_{P_1}^+(s), V_{P_2}^-(s), V_{P_2}^+(s), V_B^-(s)\}. \tag{92}$$

The velocity profile $V_o(s)$ along the whole path is shown in Fig. 34 and the corresponding vehicle slip angle $\beta_o(s)$ is shown in Fig. 35. The trajectory of the vehicle along the path is shown in Fig. 36.

The first switching from acceleration f_{GG}^{*+} to deceleration f_{GG}^{*-} is adjusted from SP_{A1} to the point ASP_{A1}. Switching control exactly at SP_{A1} results in a solution $V_e(s)$ that diverges from (92).
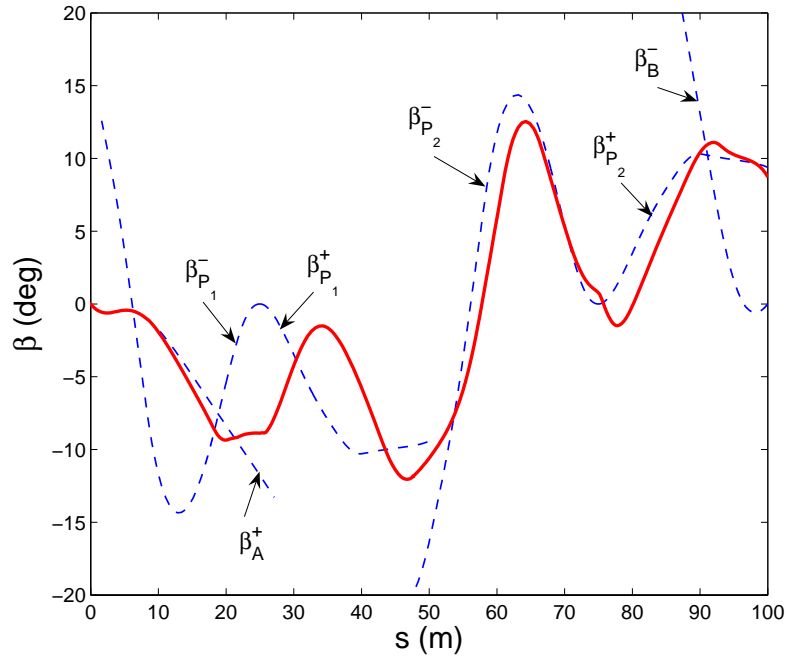
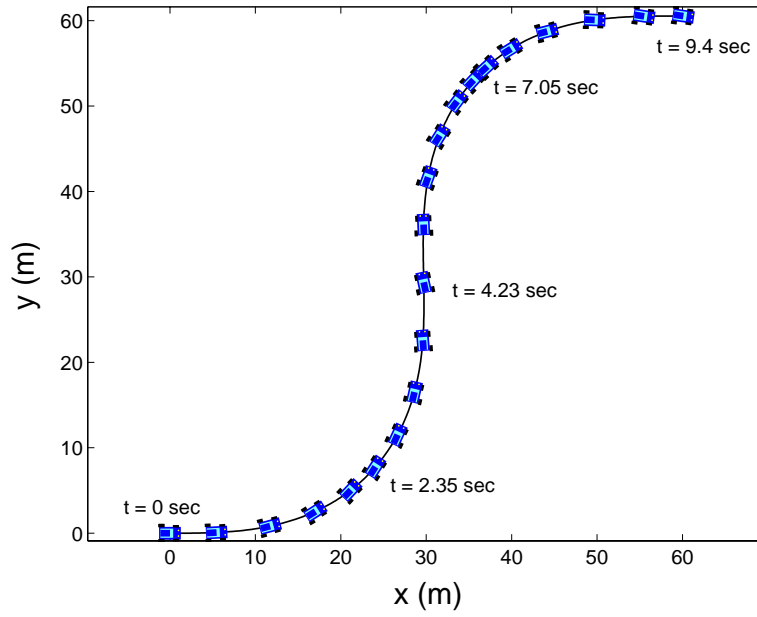Figure 35: Stable implementation to consecutive corners: vehicle slip angle.

Figure 36: Stable implementation to consecutive corners: trajectory.

3.3.8 "Zero-Slip" Implementation

In this section we present a different extension of the methodology of Section 3.2.10 to the half-car model. This time we impose the additional constraint that the vehicle tracks the path with zero slip angle in order to completely eliminate the need for yaw stability considerations.

For exact tracking of the curvature profile $\kappa(s)$ with vehicle slip angle $\beta = 0$ the centripetal force on the vehicle is given by

$$f_n = \kappa m v^2 = f_{Fy} + f_{Ry}. \tag{93}$$

For $\beta = 0$ we have that the path angle ϕ coincides with the yaw angle ψ of the vehicle. That is for $\beta = 0$

$$\psi(s) = \phi(s), \quad \psi'(s) = \phi'(s) = \kappa(s), \quad \psi''(s) = \phi''(s) = \kappa'(s). \tag{94}$$

Notice that

$$\ddot{\psi} = \psi'' v^2 + \psi' v' v. \tag{95}$$

The yaw dynamics (59) can then be written as

$$I_z \psi'' v^2 + I_z \psi' v' v = \ell_F f_{Fy} - \ell_R f_{Ry}, \tag{96}$$

or using (93)

$$I_z \psi'' v^2 + I_z \psi' v' v = \ell_F \kappa m v^2 - (\ell_F + \ell_R) f_{Ry}. \tag{97}$$

Consider now the longitudinal dynamics

$$m \dot{v} = f_t \Rightarrow m v v' = f_t. \tag{98}$$

Equation (97) can now be written as

$$I_z \kappa' v^2 + I_z \kappa \frac{f_t}{m} = \ell_F \kappa m v^2 - (\ell_F + \ell_R) f_{Ry} \Rightarrow$$
$$f_t = \frac{m(\ell_F \kappa m v^2 - I_z \kappa' v^2)}{I_z \kappa} - \frac{m(\ell_F + \ell_R)}{I_z \kappa} f_{Ry}. \tag{99}$$

Equation (99) above provides the necessary tangential force f_t for the vehicle to track $\kappa(s)$ with $\beta = 0$, given the rear lateral force f_{Ry}. The linear map $f_t(f_{Ry})$ of (99) is shown in Fig. 37.

The rear tire lateral slip with $\beta = 0$ is given by

$$s_{Ry} = -\frac{\dot{\psi} \ell_R}{v} = -\frac{\psi' v \ell_R}{v} = -\kappa \ell_R, \tag{100}$$

and the rear lateral force changes with $s_{Rx} \in [-1, +1]$ as in Fig. 21. Accordingly we can find the range of f_t using (99).

For a given operating condition of the vehicle v, $\dot{\psi}$, ($\beta = 0$), i.e. for a given value of s_{Ry}, each value of $s_{Rx} \in [-1, +1]$ corresponds to unique values of f_{Rx} and f_{Ry} from (61) and a unique value of f_t from (99). The front tire longitudinal force f_{Fx} is given by

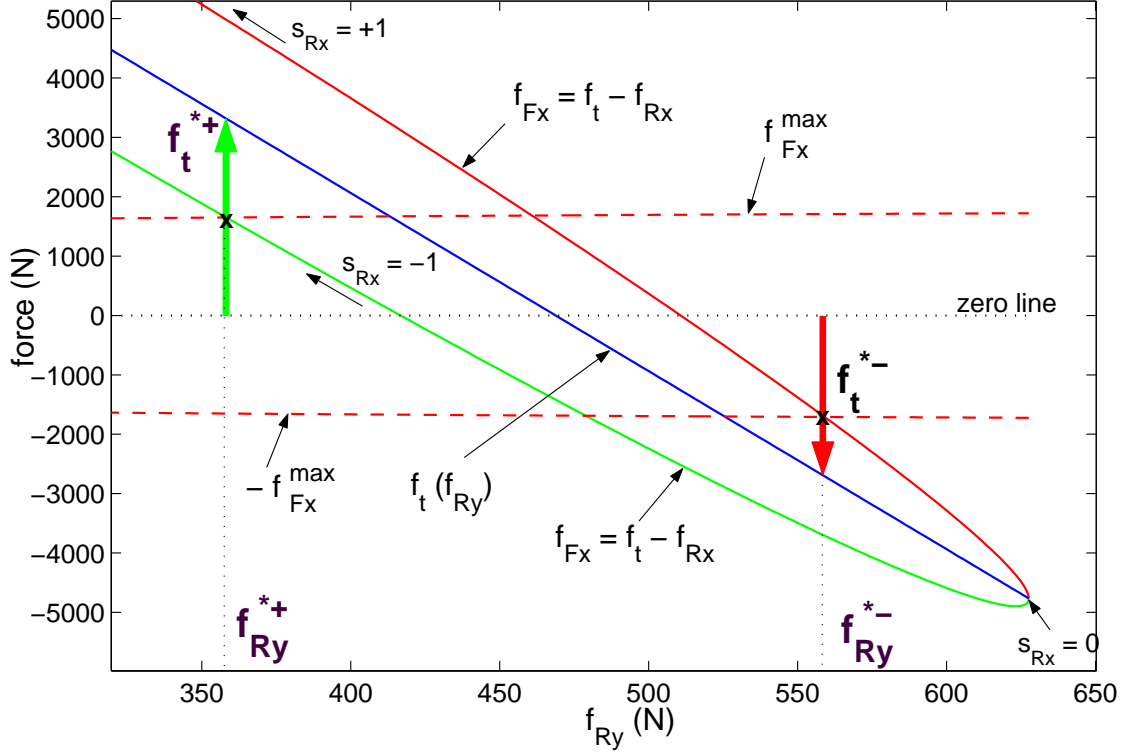$$f_{Fx}(f_{Rx}, f_{Ry}) = f_t(f_{Ry}) - f_{Rx}. \tag{101}$$

Figure 37: Forces diagram for tracking with $\beta = 0$.

The front longitudinal forces $f_{Fx}(f_{Rx}, f_{Ry})$ from (101), for $s_{Rx} \in [-1, +1]$ are shown in Fig. 37.

Finally, in order for the front tire friction force to remain in the front tire friction circle we have to ensure that

$$|f_{Fx}| \leq \sqrt{(f_F^{\max})^2 - f_{Fy}^2} = \sqrt{(f_F^{\max})^2 - (f_{Ry} - \kappa m v^2)^2} \triangleq f_{Fx}^{\max}. \tag{102}$$

The bounds $\pm f_{Fx}^{\max}$ from (102) are shown in Fig. 37.

An extension of the methodology of Section 3.2.10 to a half-car model tracking a prescribed path $\kappa(s)$ with vehicle slip angle $\beta = 0$ becomes evident.

The maximum available accelerating front longitudinal force f_{Fx} is given by the intersection of f_{Fx} from (101) with $f_{Fx}^{\max}$ from (102). This defines f_{Ry}^{*+} as in Fig. 37 which provides the maximum available accelerating force of the vehicle f_t^{*+}. The control f_t^{*+} corresponds to the maximum acceleration $u = +1$ for the point mass model of Section 3.2.10. If there is no intersection of f_{Fx} from (101) with $f_{Fx}^{\max}$ from (102) the maximum available acceleration f_t^{*+} is given for $s_{Rx} = -1$ as in Fig. 38(a).

Equivalently, the maximum available decelerating front longitudinal force f_{Fx} is given by the intersection of f_{Fx} from (101) with $-f_{Fx}^{\max}$ from (102). This defines f_{Ry}^{*-} and f_t^{*-}. The control f_t^{*-} corresponds to the maximum deceleration $u = -1$ for the point mass model of Section 3.2.10. If there is no intersection of f_{Fx} from (101) with $-f_{Fx}^{\max}$ from (102) the maximum available deceleration f_t^{*-} is given for $s_{Rx} = 0$ as in Fig. 38(b).

As velocity decreases, f_t for $s_{Rx} = \pm 1$ becomes negative, which implies a negative maximum accelerating force $f_t^{*+} < 0$ as in Fig. 39(a). Equivalently, as velocity increases, f_t for $s_{Rx} = 0$ becomes negative, which implies a positive maximum decelerating force $f_t^{*-} > 0$ as in Fig. 39(b).
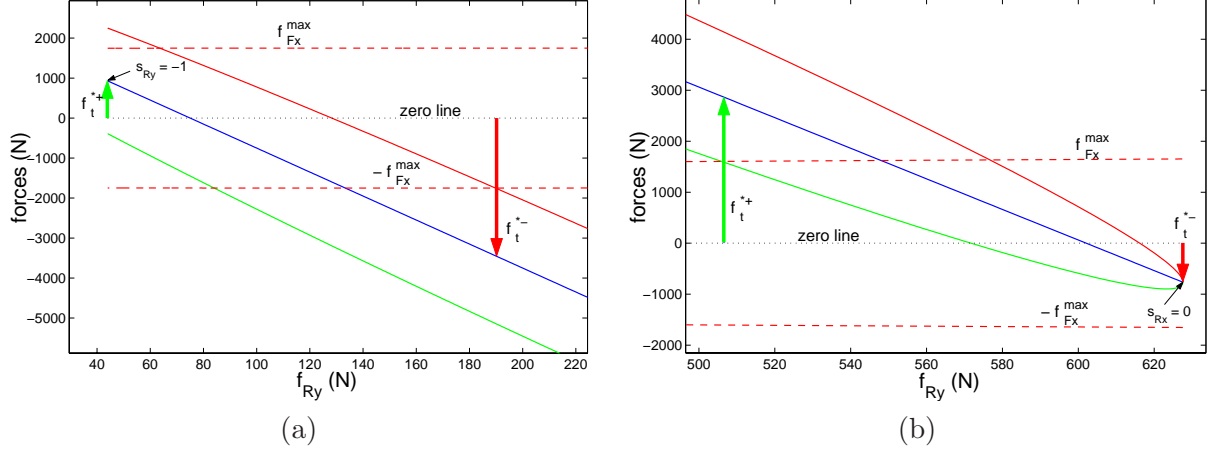
Figure 38: (a) f_t^{*+} for $s_{Ry} = -1$. (b) f_t^{*-} for $s_{Ry} = 0$.

In order to avoid such problematic cases we switch from $f_t^{*\pm}$ to the following control

$$f_t = 0, \quad \text{when} \quad f_t^{*-} > 0 \quad \text{or} \quad f_t^{*+} < 0. \tag{103}$$
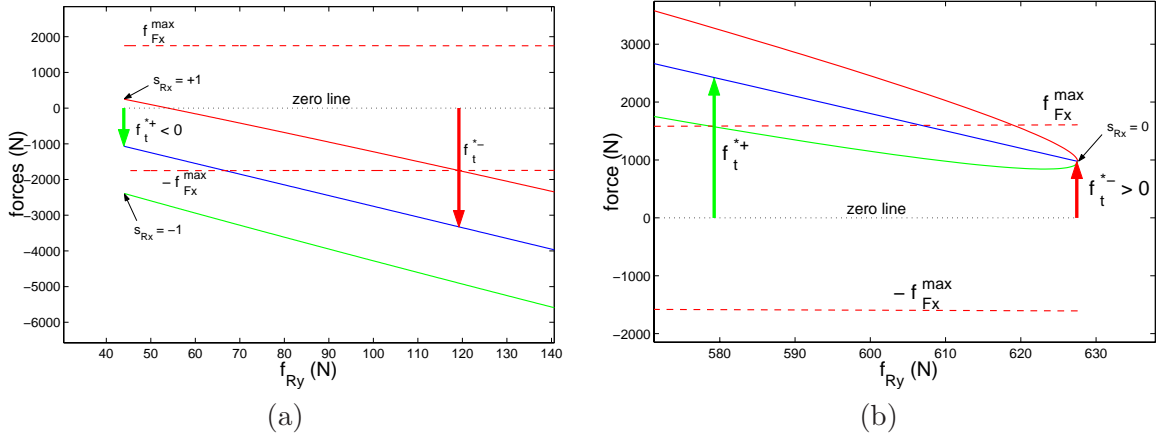

Figure 39: (a) Negative maximum acceleration f_t^{*+} (b) Positive maximum deceleration f_t^{*-}.

3.3.9 Numerical Example: Zero-Slip Implementation

Consider the path of Fig. 33. This time we calculate the trajectory of the vehicle using the zero-slip strategy of Section 3.3.8.

First we need to derive the optimal states at the points of minimum magnitude of radius P_1 and P_2. As for the whole trajectory we take $\beta(s_{P_1}) = \beta(s_{P_2}) = 0$. From equations (94) we get

$$\dot{\psi}(s_{P_i}) = \psi'(s_{P_i})v(s_{P_i}) = \kappa(s_{P_i})v(s_{P_i}), \quad i = 1, 2. \tag{104}$$

To maximize the centripetal force at P_1 and P_2 we enforce $s_{Rx}(s_{P_i}) = 0$, $i = 1, 2$ to maximize f_{Ry} which lies along the normal direction n. The rear lateral force is calculated from (61), given $s_{Ry} = -\kappa \ell_r$. The initial velocity $v(s_{P_i})$, $i = 1, 2$ is calculated then from (99) setting $f_t = 0$.

The optimization scheme of Section 3.3.7 is repeated here using f_t^{*+} for maximum acceleration and f_t^{*-} for maximum deceleration. The resulting velocity profile (Fig. 40) reveals that the "zero-slip" implementation of Section 3.3.8 is conservative compared to the "stable" implementation of Section 3.3.7. Stability and continuity of the yaw states is however a-priori guaranteed in the "zero-slip" strategy. Figure 41 shows the calculated trajectory.
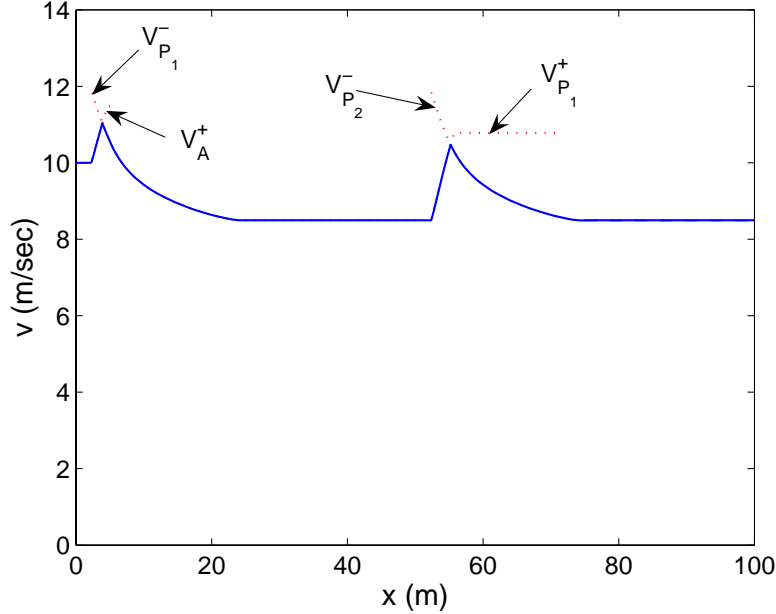

Figure 40: Zero-slip implementation to consecutive corners: velocity profile.

3.4 Conclusions and Future Work

In this work we presented semi-analytic methodologies to generate optimal and near-optimal minimum time velocity profiles for ground vehicles along a prescribed path.

First, we presented the point mass model case and a constructive proof of optimality of the minimum time solution. The methodology accounts for the loss of controllability due to the coupling of accelerating/braking with centripetal forces. In addition, the necessary optimality conditions were derived, which provide an estimate of the number and type of control switchings according to the geometry of the prescribed path. A receding horizon scheme has also been proposed to lower the computational cost of implementing the proposed analytic approach, and to account for unpredictable changes in the environment. Numerical simulations show that the proposed on-line velocity optimizer is competitive when compared to lap times obtained by expert F1 race drivers.

Next, we presented several extensions of the point mass case methodology to a vehicle model that includes the yaw dynamics. We introduced a half-car model and calculated the acceleration enveloped from the tire friction forces on the front and rear axles. Direct implementation of the point mass control strategy to the half-car model case revealed the need to design control schemes taking yaw stability into consideration. We followed two different approaches towards a stable with respect to yaw dynamics implementation. In the first approach we designed a control scheme that intervene during execution of the optimal maximum acceleration/maximum deceleration action when the vehicle oversteers and the yaw dynamics tend to instability. In the second approach we
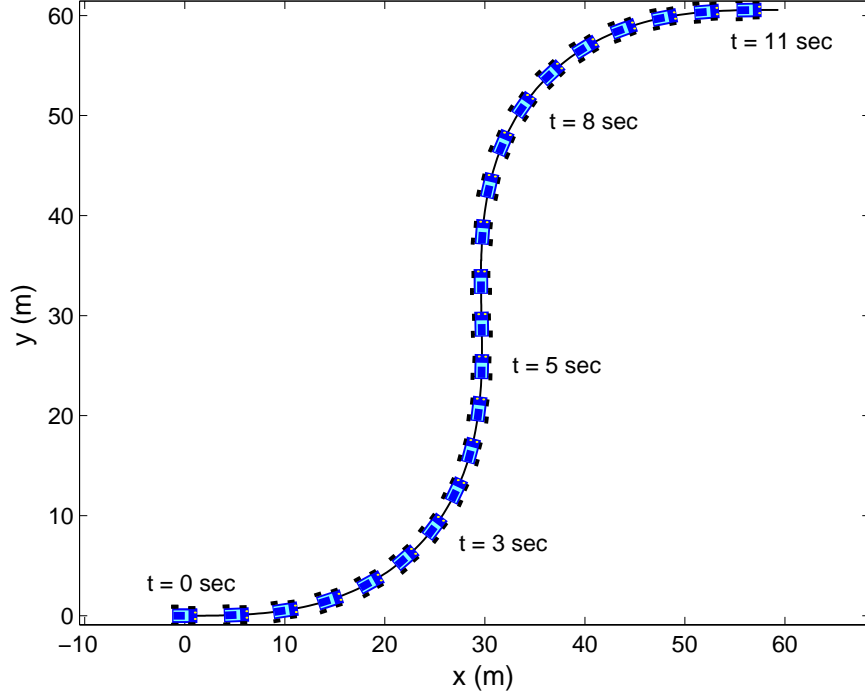
Figure 41: Zero-slip implementation to consecutive corners: trajectory.

redefined the maximum acceleration limits of the vehicle subject to the additional constraint of zero vehicle slip angle throughout the path.

The zero-slip implementation of the point-mass methodology to the half-car completely eliminates the problems associated with yaw stability. Preliminary results presented above, however, show that the zero-slip implementation generates conservative results. To this end we will continue towards developing a stable implementation scheme according to Section 3.3.4 that will compensate for both oversteer and understeer of the vehicle.

Ultimately we plan to develop a hybrid numerical/semi-analytic optimization scheme to calculate optimal trajectories for ground vehicles. The semi-analytic methodologies presented in this work can be used to provide the necessary initial guesses to numerical optimization schemes, which allow for further increase in the fidelity of the vehicle models used and generate realistic results.

References

[1] J. Hendrikx, T. Meijlink, and R. Kriens, "Application of optimal control theory to inverse simulation of car handling," *Vehicle System Dynamics*, vol. 26, pp. 449–461, 1996.

[2] D. Casanova, R. S. Sharp, and P. Symonds, "Minimum time manoeuvring: The significance of yaw inertia," *Vehicle System Dynamics*, vol. 34, pp. 77–115, 2000.

[3] D. Casanova, R. S. Sharp, and P. Symonds, "On minimum time optimisation of formula one cars: The influence of vehicle mass," in *Proceedings of AVEC 2000*, (Ann-Arbor, MI), August 22-24 2000.

[4] E. Velenis and P. Tsiotras, "Minimum time vs maximum exit velocity path optimization during cornering," in *2005 IEEE International Symposium on Industrial Electronics*, (Dubrovnic, Croatia), pp. 355–360, June 20 - 23 2005.

[5] M. Spenko, *Hazard Avoidance for High-Speed Rough-Terrain Unmanned Ground Vehicles*. Department of Mechanical Engineering, Massachusetts Institute of Technology: PhD thesis, 1995.

[6] D. Metz and D. Williams, "Near time-optimal control of racing vehicles," *Automatica*, vol. 25, no. 6, pp. 841–857, 1989.

[7] M. Gadola, D. Vetturi, D. Cambiaghi, and L. Manzo, "A tool for lap time simulation," in *Proceedings of SAE Motorsport Engineering Conference and Exposition*, (Dearborn, MI), 1996.

[8] M. Lepetic, G. Klancar, I. Skrjanc, D. Matko, and B. Potocnic, "Time optimal path planning considering acceleration limits," *Robotics and Autonomous Systems*, vol. 45, pp. 199–210, 2003.

[9] J. Bobrow, S. Dubowsky, and J. Gibson, "On the optimal control of robotic manipulators with actuator constraints," in *Proceedings of the American Control Conference*, (San Francisco, CA), pp. 782–787, June 1983.

[10] J. Bobrow, S. Dubowsky, and J. Gibson, "Time-optimal control of robotic manipulators along specified paths," *International Journal of Robotics Research*, vol. 4, no. 3, pp. 3–17, 1985.

[11] K. Shin and N. McKay, "Minimum-time control of robotic manipulators with geometric path constraints," *IEEE Transactions on Automatic Control*, vol. 30, no. 6, pp. 531–541, 1985.

[12] T. Schouwenaars, B. De Moor, E. Feron, and J. How, "Mixed integer programming for multi-vehicle path planning," in *Proceedings of the 2001 European Control Conference*, (Porto, Portugal), pp. 2603–2608, September 2001.

[13] J. Bellingham, A. Richards, and J. How, "Receding horizon control of autonomous aerial vehicles," in *Proceedings of the American Control Conference*, (Anchorage, AK), pp. 3741–3746, May 8-10 2002.

[14] T. Schouwenaars, E. Feron, and J. How, "Safe receding horizon path planning for autonomous vehicles," in *Proceedings of the 40th Allerton Conference on Communication, Control and Computing*, (Monticello, IL), October 2002.

[15] A. T. van Zanten, R. Erhardt, and G. Landesfeind, K. Pfaff, "Vehicle stabilization by the vehicle dynamics control system ESP," in *IFAC Mechatronic Systems*, (Darmstadt, Germany), pp. 95–102, 2000.

[16] K. Koibuchi, M. Yamammoto, Y. Fukada, and S. Inagaki, "Vehicle stability control in limit cornering by active brake," *SAE Special Publications, Investigations and Analysis in Vehicle Dynamics and Simulation*, no. 1141, pp. 163–173, 1996.

[17] Anonymous, "RT3000 inertial and GPS measurement system, report from Silverstone F1 test," Technical Report, Oxford Technical Solutions, Oxfordshire, UK, 2002.

[18] E. Bakker, L. Nyborg, and H. Pacejka, "Tyre modelling for use in vehicle dynamics studies," 1987. SAE Paper No. 870421.

[19] W. Milliken and D. Milliken, *Race Car Vehicle Dynamics*. Warrendale PA USA: Society of Automotive Engineers (SAE) International, 1995.

[20] S. Skiena, *The Algorithm Design Manual*. New York: Springer-Verlag, 1997.

[21] T. Gillespie, *Fundamentals of Vehicle Dynamics*. Warrendale PA USA: Society of Automotive Engineers (SAE) International, 1992.